Spin-Motive Force
— Giving Faraday's Law a New Spin —

Faraday's law of induction is a basic principle of physics which explains an electromotive force that drives electrical currents in generators and transformers. Recently, it has been revealed that, in magnetic materials, there is a correction to this law, which can be elegantly restated in terms of the time rate of change of the so-called "Berry phase" [1].

Electrical currents usually correspond to a flow of electrons, elementary particles that carry a tiny electrical charge, $-e$. In 1930, Dirac showed that, in order to be consistent with Einstein's special relativity and quantum mechanics, an electron must also have "spin," in effect, being a tiny magnet (Fig.1). "Spintronics" is an emerging electronics technology in which the electron spin is used in an essential manner [2]. The issues studied in this field include tunneling magnetoresistance, domain wall motion due to magnetic fields or electric currents in ferromagnets [3], and the spin-Hall effect in paramagnetic metals with strong spin-orbit interaction such as Pt and Au, aiming at controlling the spin degrees of freedom.

One of the versatile methods to generate electric power for driving various electronic devices is Faraday's law of induction, a fundamental principle dating from 1831. The usual Faraday's law determines an electromotive force ε as

$$\varepsilon = -d\Phi/dt,$$

where Φ is the magnetic flux. To derive this law, only forces resulting from the charge of electrons have been accounted for. In ferromagnetic materials, however, there exist nonconservative "spin forces" which also contribute to ε. These might be included in Faraday's law if Φ is replaced by $[\hbar/(-e)]\gamma$,

$$\varepsilon = -[\hbar/(-e)]d\gamma/dt,$$

where $\gamma = \gamma_e+\gamma_s$ is a "Berry phase." $\gamma_e = [(-e)/\hbar]\Phi$ recovers the usual charge part of Faraday's law while γ_s reflects the spin contribution suitably averaged over the electron spin direction. These contributions to ε represent the requirements of energy conservation in itinerant ferromagnets with time dependent magnetization. This is an extremely common situation, for example, the situation in an every-day power transformer. It has more important implications in connection with spintronics.

A Berry phase is a geometric phase, which appears ubiquitously in the context of condensed matter physics, optics, quantum computation, *etc*. The spin Berry phase γ_s

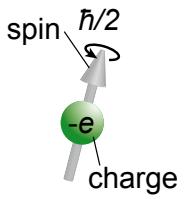

Fig. 1. An electron has charge and spin degrees of freedom.

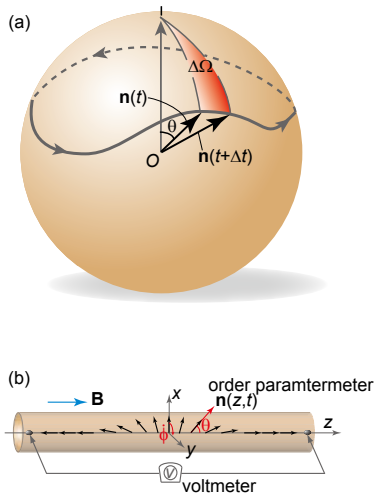

Fig. 2. (a) A geometrical aspect of a spin Berry phase. (b) A ferromagnetic wire containing a domain wall. Black arrows indicate the direction of the order parameter (magnetization).

for an electron is $-\Omega/2$, where Ω is the solid angle subtended by the path of the order parameter **n** in spin space, as illustrated in Fig. 2(a). The simple example, see Fig. 2(b), is a ferromagnetic wire which lies along the z direction and which contains a single domain wall, a transition region connecting two magnetic domains. The ferromagnetic order parameter is indicated by the black arrows and the unit vector $\mathbf{n}(z,t)$. This defines the direction of the internal exchange field which is specified by two angles, θ and φ. For a DC magnetic field **B** along the z axis, the wall starts to precess so that it develops a time dependent solid angle, $d\Omega/dt = \pm 4\mu B/\hbar$, for conduction electrons traversing the wire. The + (-) sign corresponds to spin-up (-down) of the electrons. This generates a "spin-motive force" $\varepsilon_s^{\pm} = \pm 2\mu B/e$, and hence, an electromotive force $\varepsilon = 2p\mu B/e$, where p is a spin polarization of the ferromagnet. The magnitude is evaluated for typical itinerant ferromagnets, *e.g.*, $Ni_{81}Fe_{19}$, ε ~ 100 [μV/T].

While the corrections are small for traditional electric machines, they embody the requirements of energy conservation for the spintronic devices being developed by IBM, Freescale, and Hitachi. In more general terms, the correction to Faraday's law can be demonstrated conclusively for the first time in terms of the Berry phase.

References

[1] S. E. Barnes and S. Maekawa, Phys. Rev. Lett. **98**, 246601 (2007).

[2] S. E. Barnes, J. Ieda, and S. Maekawa, Appl. Phys. Lett. **89**, 122507 (2006).

[3] M. Yamanouchi, J. Ieda, F. Matsukura, S. E. Barnes, S. Maekawa, and H. Ohno, Science **317**, 1726 (2007).

Contact to
Sadamichi Maekawa (Theory of Solid State Physics Division)
e-mail: maekawa@imr.tohoku.ac.jp

Direct Observation of Field-induced Variant Transformation in Fe_3Pt Using Pulsed Magnetic Field X-ray Diffraction

A field induced variant transformation and its dynamical response have been measured by combining a fast sweeping high magnetic field and a synchrotron X-ray. It is confirmed that a variant can rotate in a short time of msec range.

A time resolved synchrotron X-ray diffraction is one of powerful tools to investigate a material response triggered by extreme parameter such as high magnetic fields. A dynamical behavior of martensitic transformation has attracted much attention because of the possible application as a fast actuator. An example is found in the giant magnetic-field-induced strain of the ordered Fe_3Pt alloy. However, the direct observation of the variant transformation has been difficult and thus the response of the variant has not been known so far.

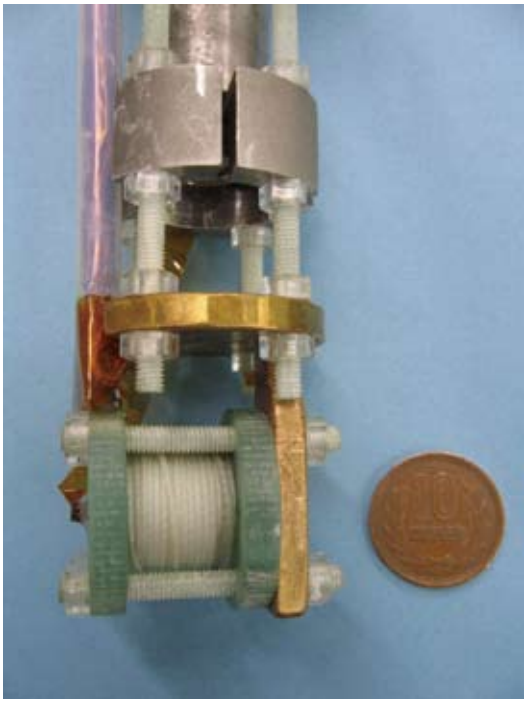

Fig. 1 A small pulsed magnet used to observe the variant transformation in fast sweeping high magnetic field. A magnetic field of msec pulse duration can be generated.

In the present work, we have developed a novel technique to investigate the field induced martensitic phase transition. Figure 1 shows the mini magnet used for time resolved X-ray diffraction experiment in a fast sweeping magnetic field. Thanks to the extremely small size, the magnet and the capacitor bank are portable and thus the combination with X-ray diffractometer becomes possible. In fact, the capacitor bank is as small as a small refrigerator and the storing energy is only 2 kJ. An advantage of such small system is that a magnetic field sweep rate can be varied up to 1.9×10^3 T/s.

The first experiment wad made to study the giant magnetic-field-induced strain in the martensitic phase of ordered Fe_3Pt alloy. Figure 2 shows the time dependence of the ω-scan profile of the sample. Two different variants are observed as two distinct peaks. The intensity of the right peak decreases with increasing magnetic fields. It is the first direct evidence of the field induced rearrangement of the variants (crystallographic domains) in pulsed magnetic fields. The decrease of the right peak intensity is caused by the rotation of the variants from the c axis perpendicular to the magnetic field to the c axis parallel to the magnetic field. Moreover, we found that the reorientation behaviors are different for different variants with the same crystallographic direction. The results demonstrate the crucial importance of microscopic investigation, such as X-ray diffraction analysis, of the martensitic transition.

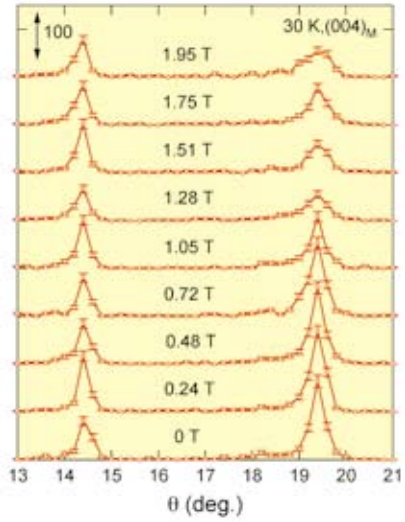

Fig. 2 The field dependence of ω-scan profile of Fe_3Pt alloy in fast sweeping magnetic fields. The right peak looses the intensity for variant transformation.

We examined the sweeping speed dependence of the variant rotation and found that the variant follows the pulsed field of up to 1.9×10^3 T/s. It indicates that the Fe_3Pt has the sub-msec response to the magnetic fields.

Reference

[1] Z. W. Ouyang, Y. H. Matsuda, H. Nojiri, T. Inami, K. Ohwada, M. Tsubota, T. Sakon, T. Fukuda, and T. Kakeshita, J. Appl. Phys. **102**, 113917 (2007).

Contact to
Hiroyuki Nojiri (Magnetism Division)
e-mail: nojiri@imr.tohoku.ac.jp

GaN Integration on Si via Symmetry-Converted Silicon-on-Insulator

Integration of metals and semiconductors having 3- or 6-fold symmetry on device-oriented (i.e., (001)) silicon wafers, which have 4-fold symmetry, has been a longstanding challenge. We demonstrate that, by using symmetry-converted (111) silicon-on-insulator, we can integrate wurtzite-structure gallium nitride, which has 3-fold symmetry, with Si(001). This technique would enable the commercial integration of wide-ranging important materials onto Si (001) base wafers.

Silicon serves as the fundamental material for the semiconductor industry because of its superior processability in the fabrication of various device structures, and especially because of its ability to form a high-quality oxide. Si(001), with a square surface lattice, has been used for actual device fabrication primarily because of the lower interface state density. A major and important class of materials having 3- or 6-fold symmetries has intrinsic difficulty growing on Si(001), because the symmetry mismatch at the interface induces roughness and polycrystallization, factors that seriously degrade electronic and optoelectronic performance. A general solution for this long-standing problem is given by utilizing a silicon-on-insulator (SOI) structure where a thin Si(111) layer is bonded to Si(001) via the oxide layer. A wurtzite GaN film is directly grown on this SOI structure to demonstrate the validity of our approach. [1]

The wurtzite structure of GaN has a freedom in its polarity, which in turn has direct influence on surface structure, growth process, and its quality. In case of non-polar substrate like Si, it is especially important to control the nucleation stage to accomplish mono-polar film with atomically smooth surface. The GaN films grown on Si(111) substrates with the N-rich nucleation condition exhibit 3x3, 6x6, and c(6x12) reconstructions in their scanning tunneling micrographs (STM), all typical of the surface structures for N-polar GaN films, as shown in Fig. 1(a). [2] This indicates that the surface is covered uniformly with N-polar film without forming inversion domain wall. On the other hand, the nucleation under Ga-rich conditions results in formation of a rougher surface after the completion of the film growth, and very flat Ga-fluid areas over Ga-polar crystal coexisting with the N-polar c(6x12) reconstructed areas can be seen in the STM images (Fig. 1(b)). [2] These results indicate that N-rich condition in the nucleation layer growth stage is critical for achieving the growth of mono-polar GaN films on Si(111) without inversion domain boundaries. An improved polarity control has been achieved by inserting a ZrB_2 buffer layer at the interface. [3]

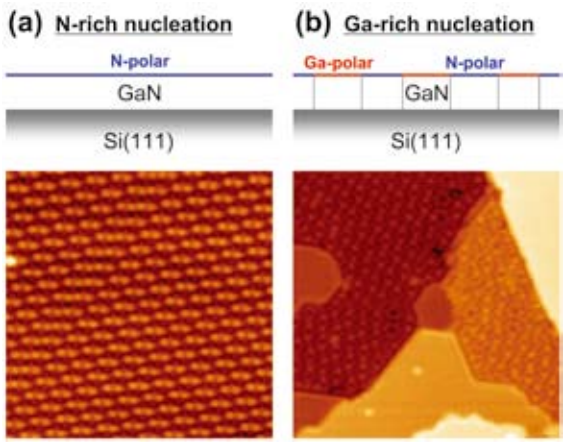

Fig. 1. Scematic drawings together with corresponding STM images (25 x 25 nm^2) of wultzite GaN films grown directly on Si(111) substrates with (a) N-rich and (b) Ga-rich nucleation conditions. The N-rich condition is critical to achieve uniform film growth without forming inversion domain walls.

Making a good use of above-mentioned polarity control technique in GaN growth on Si, we integrated GaN on symmetry-converted SOI structure, as is shown in Fig. 2. [1] Ordered STM images can be observed for the Si(111)-SOI substrate and the GaN surface, which assures their microscopic uniformity as well as their uniform connectivity on the insulating oxide layer to the end of the specimen. The stability of the orientation converted SOI on Si(001) observed here would enable general integration of the intriguing class of materials with 3- or 6-fold surface symmetries on actual Si devices.

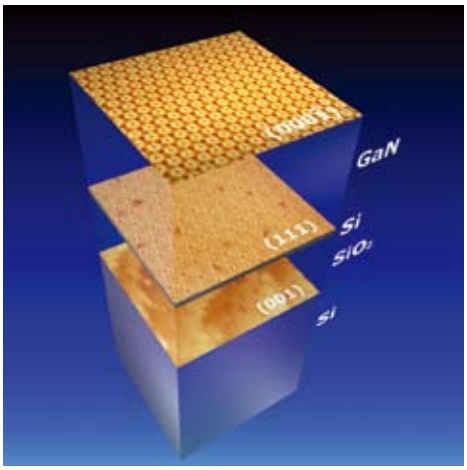

Fig. 2. Schematics of symmetry converted growth of GaN on Si(001) with superimposed STM images (25 x 25 nm^2) observed in this work. GaN is grown on a 7x7 clean surface formed on a Si(111) template layer bonded with Si(001) handle wafer via SOI structure. An ordered 6x6 reconstructed surface appears as a consequence of excess Ga termination of grown film, showing uniform formation of a N-polar GaN film. Removal of the SOI structure by heating at 1300 °C results in the formation of the Si(001) dimer-row structure, having square-base surface lattice.

References

[1] Y. Fujikawa, Y. Yamada-Takamura, G. Yoshikawa, T. Ono, M. Esashi, P. P. Zhang, M. G. Lagally, and T. Sakurai, Appl. Phys. Lett. **90**, 243107 (2007).

[2] Z. T. Wang, Y. Yamada-Takamura, Y. Fujikawa, T. Sakurai, and Q. K. Xue, Appl. Phys. Lett. **87**, 032110 (2005).

[3] Y. Yamada-Takamura, Z. T. Wang, Y. Fujikawa, T. Sakurai, Q. K. Xue, J. Tolle, P.-L. Liu, A. V. G. Chizmeshya, J. Kouvetakis, and I. S. T. Tsong, Phys. Rev. Lett. **95**, 266105 (2005).

Contact to
Yasunori Fujikawa (Surface and Interface Research Division)
E-mail: fujika-0@imr.tohoku.ac.jp

Development of Scanning Neutron Diffraction and Local Structures Investigations in Stainless Steel

We applied a spatial scanning measurement technique to neutron diffraction on a powder diffractometer, and performed scanning neutron diffraction experiments to investigate local structures of materials. By this technique, we succeeded in observing distribution the strain induced martensite phase in a type-304 stainless steel plate. The comparison with the distribution of magnetization gives us information of local structures in internal regions. This method is particularly important for investigation of industrial materials because it can observe internal regions of materials,

From industrial view points, assessment of local structures in application materials are important; such as grain distribution, microcrystals, partially deposed second phases, and so on. To investigate local structures of materials, we have put the scanning neutron diffraction (SND) technique to practical use on the KINKEN neutron powder diffractometer HERMES [1]. The SND technique can obtain information on local structures of materials and its position dependence. Because neutrons have a larger penetration depth (a few cm) than X-rays, the SND technique provides structural information even in internal regions of industrial applications, while X-ray can observe only near surface regions. Note that neutrons are the unique prove to observe structures at internal regions of materials with a cm size by non-destructive observation.

Figure 1 shows a schematic view of the alignment of the apparatus of the SND experiments on HERMES, which is basically same as the scanning X-ray diffraction technique. The x-y scanning sample stage was controlled by the data acquisition system of HERMES so that a diffraction pattern at each point on the sample can be observed automatically. Since 150 ^{3}He detectors are installed on HERMES, one can obtain diffraction patterns for a short time. The beam size was reduced with the second beam narrower with a beam cross section of 2 x 5mm^2 for the present experiments of a type-304 stainless steel. The position resolution on the sample was determined by the beam size. Note that the positional resolution can be easily changed by changing the beam size.

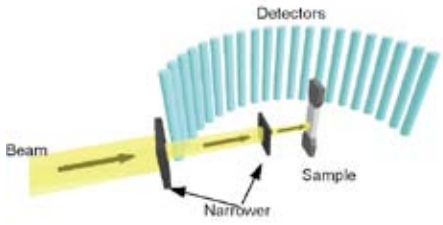

Fig.1 Schematic view of the layout of the SND experiments on HERMES [1]. The distance between the second narrower and the sample was 15mm, and between the sample and each detector was 1350mm. The sample could be automatically moved along x- and y- directions against the fixed beam.

We succeeded in observing positional dependence of diffraction patterns from small areas (approximately 2 x 5 mm^2) of a type-304 stainless steel plate with a dimension of 19.5 x 50 x 4.7mm^3 subjected to a mechanical tensile strain of 90% of the 0.2% offset yield strength. In the SND experiments, we confirmed that the crystallographic circumstance in the strain-loaded type-304 stainless steel is not homogeneous. For instance, we observed positional deviation in the grain direction of the master-alloy austenite phase, and local distribution of the stress induced martensite phase. Figure 2 shows comparison of distribution of magnetization observed by a scanning SQUID magnetometer (SSM) [2], and integrated intensity of the 211 Bragg peak from the martensite (α') phase observed by SND. Note that the martensite phase enhances mechanical hardness, and may increase the risk of cracks. Thus, assessment of the induced α' phase is important for applications. As shown in Fig.2, the larger magnetization (circles) was basically disposed around the deposition of the martensite phase (arrows), indicating that the magnetization is caused by the martensite phase. On the other hand, some regions with deposition of the martensite phase but without magnetization were observed exists; for instance x=10mm, y=25mm (indicated with the question mark). This means that the martensite phase exists in the internal region of the sample, where SSM cannot observe magnetization at the regions from the surface.

The SND technique is a particularly important probe for estimating the stress-induced phase, because it non-destructively observes even the inside of bulk materials. Moreover, by the SND technique, a single measurement can detect even unpredictable precipitation of an unknown secondary phase, in which the positions of Bragg reflections cannot be predicted. Moreover, SND on HERMES will be applicable for texture measurements of materials. The details of the SND technique have already been published elsewhere [3]. We also have applied for a patent of the SND technique on HERMES.

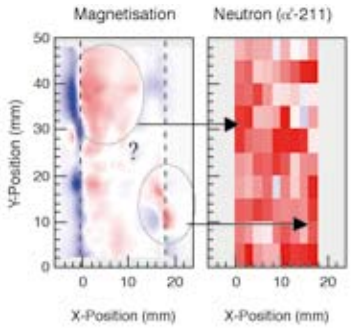

Fig.2 Distributions of magnetization observed by SSM(left), and integrated intensity of a Bragg peak from the martensite phase observed by SND of a type-304 stainless steel sample. In the magnetization (left), red and blue indicate larger positive and negative magnetizations, respectively. In the neutron intensity (right), red indicate stronger intensity.

References

[1] K. Ohoyama, T. Kanouchi, K. Nemoto, M. Ohashi, T. Kajitani and Y. Yamaguchi, Jpn. J. Appl. Phys. **37**, 3319 (1998).

[2] K. Isawa, *Superconductivity, Magnetism and Magnets* (Nova Science Publishers, New York, 2006) Chap. 10.

[3] K. Ohoyama, K. Isawa, K. Yamada, Jpn.J. Appl. Phys. **46**, 7925 (2007).

Contact to
Kenji Ohoyama (Neutron and γ-Ray Spectroscopy on Condensed Matters Division)
e-mail: ohoyama@imr.tohoku.ac.jp

Defect Dynamics in Silicon under High Magnetic Field

Dislocations lead to spatial variations in electrical and optical properties and also degradation of semiconductor devices. Thus, a great deal of effort is being made in clarifying dislocation properties and dislocation-impurity interactions under various applied fields as temperature, stress, current, light, and so forth. However, far less is known of the influences or modifications of dislocation activities by a magnetic field.

Utilization of a high magnetic field has received keen attention for development of various devices incorporating magnetic, superconductive, spintronic materials, and also some semiconductors. Knowledge of the influences against or modifications of defect properties and structures accompanying atomic displacements by an external magnetic field, however, is even now quite limited except for some works on a concept of magneto-plastic phenomena in impure ionic crystals, metals, and alloys. In such crystals, dislocations become mobile, resulting in reduction of their mechanical strength. Herein, such phenomena and relevant mechanisms are discussed in terms of dislocation motion and solid-state reaction, *i.e.*, the spin-dependent release of dislocations from segregated paramagnetic impurity centres/complexes and the subsequent relaxed motion of dislocations in matrix crystals, leading to enhancement of plasticity.

Impurity oxygen (O) in semiconductor silicon (Si) is well known to have a strong effect of pinning/locking of dislocations due to preferential segregation and formation of complexes at elevated temperatures. Thus, it is quite interesting to clarify how high magnetic field affects on the dislocation-impurity interaction in the most typical semiconductor Si. Indeed, we investigated magnetic effects on dislocation-oxygen impurity interaction in Czochralski (CZ) grown Si containing oxygen in a concentration of ~10^{18} cm^{-3} under a high magnetic field up to 10 T at elevated temperatures.

Specimens prepared from an undoped CZ-Si were pre-annealed at 650˚C for 1 hour and subsequently were treated at the same temperature under an application of magnetic field up to 8 T for duration from 15 min to 2 hours in a furnace installed into a cyclo-cooled superconducting magnet (11T-CSM) in the High Field Laboratory for Superconducting Materials, Institute for Materials Research, Tohoku University. After removed from the furnace at RT, the specimens were stressed at 650˚C in a vacuum by means of three-point bending.

Fig. 1 shows the variation in the critical stress for dislocation generation against the duration of the magnetic field application of 1 and 8 T at 650˚C together with that of critical stress for dislocation generation in specimens treated without magnetic field 0T. The dashed green line shows the critical stress level for dislocation generation in the as-grown specimen. Under the both intensities of the magnetic field, the magnitude of the critical stress first increases to a maximum and then decreases probably to the stress level of as-grown specimen, while the specimens treated without magnetic field show a little increase in the critical stress, probably due to additional annealing effect. The maximum of the critical stress ≈ 15 MPa is comparable for the both intensities of magnetic field. It is seen that the treatment under application of the higher intensity of magnetic field leads to the more prompted variation of the critical stress. These results imply that the magnetic treatment under ≈ 1 T for 1 hour and under ≈ 8 T for 15 min at 650˚C most effectively suppresses dislocation generation from the scratch. However, the prolonged magnetic- treatment leads to disappearance of such effect.

The critical stresses for dislocation generation of float-zone (FZ) grown Si specimens are almost zero, irrespective of the magnetic-treatments. This implies that there is no effect of magnetic treatment in FZ-Si. Thus, it is supposed that the observed variation in the critical stress is originating from the magnetic field application on dislocation generation in only CZ-Si, *i.e.*, containing O impurity.

It is found that generation of dislocations was effectively suppressed under certain conditions of the magnetic treatments. The underlying microscopic nature induced by application of high-magnetic field is complicated at present. The details of dislocation-impurity interaction in Si should be clarified experimentally as well as theoretically, for understanding basic natures and kinematics of the spin-dependent solid-state reaction in a future. Here, it should be emphasized that spin-dependent reaction should be useful for improving semiconductor device efficiency through controlling atomic configuration, displacement of defects, accumulation of harmful metallic impurities.

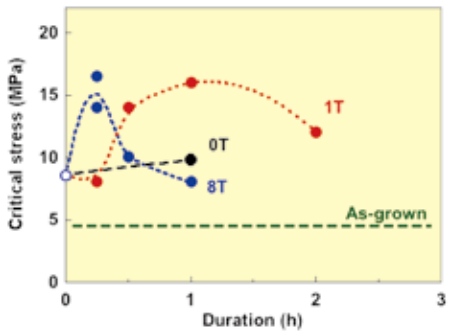

Fig. 1. Variation in the critical stress for generation of 60˚ dislocations against the duration of the magnetic treatment at 650˚C in Si crystals. The critical stress for dislocation generation in the as-grown Si crystal is superimposed.

References

[1] I. Yonenaga and K. Takahashi, J. Appl. Phys. **101**, 053528 (2007).

[2] I. Yonenaga, K. Takahashi, T. Taishi, and Y. Ohno, Physica B **401-402**, 148 (2007).

Contact to
Ichiro Yonenaga (Physics of Crystal Defects Division)
e-mail: yonenaga@imr.tohoku.ac.jp

Manifestation of Precipitation Induced Recrystallization During Plasma-Nitriding of Fe-Cr Alloys

This article reviews precipitation induced recrystallization (PIR) phenomenon in plasma-nitriding of Fe-Cr alloys discovered recently. When Fe-Cr alloys are nitrided in an appropriate condition, new ferrite grains composed of (ferrite + CrN) lamellae holding specific orientation relationship with original ferrite grains are formed in the nitrided zone without any mechanical-deformation treatment.

Fig. 1 shows a cross-sectional SEM image and the corresponding ferrite orientation map of the Fe-18Cr alloy nitrided at 843K for 18ks [1]. The area with bright contrast in a left hand side corresponds to the nitrided zone in (a). In the orientation map, columnar-shaped ferrite grains which are elongated along the nitriding direction and exhibit orientations different from that of the original ferrite grains are seen. Crystallographic analysis reveals that most of newly formed ferrite grains hold Σ9 coincide site lattice relation, represented by 38.9º rotation around <110>α, with respect to the original ferrite grains within a deviation of 5º. Those new ferrite grains consist of very fine (ferrite + CrN) lamellar structure. Based on detailed TEM observation, we proposed that ferrite formation is caused by specific recrystallization process induced by volumetric mismatch between CrN continuously precipitated and the ferrite matrix. We named this phenomenon as precipitation induced recrystallization (PIR). Subsequent discontinuous precipitation at the grain boundary between the recrystallized and original ferrite grain forms (ferrite + CrN) lamellar structure. Fig. 2 summarizes the effect of a Cr content and a nitriding temperature on the appearance of PIR in plasma-nitrided Fe-Cr alloys [2]. Clearly, PIR tends to appear at a higher Cr content and a lower nitriding temperature.

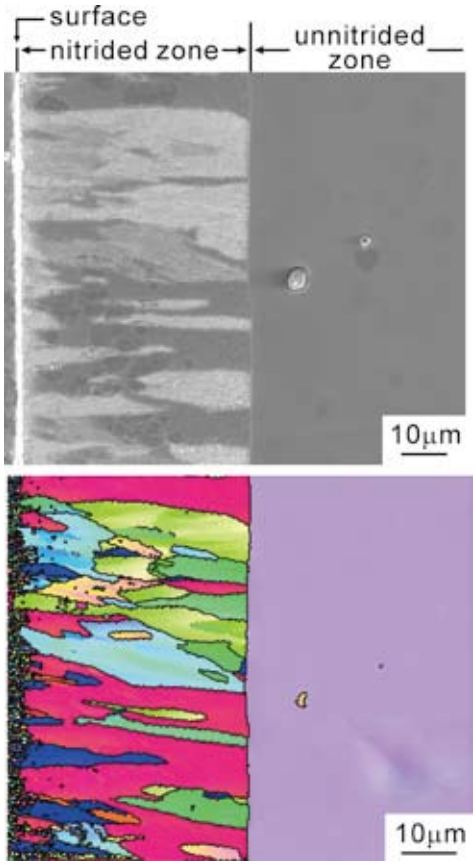

Fig. 1 SEM image and corresponding ferrite orientation map of a cross section of the Fe–18Cr alloy nitrided at 843 K for 18 ks.

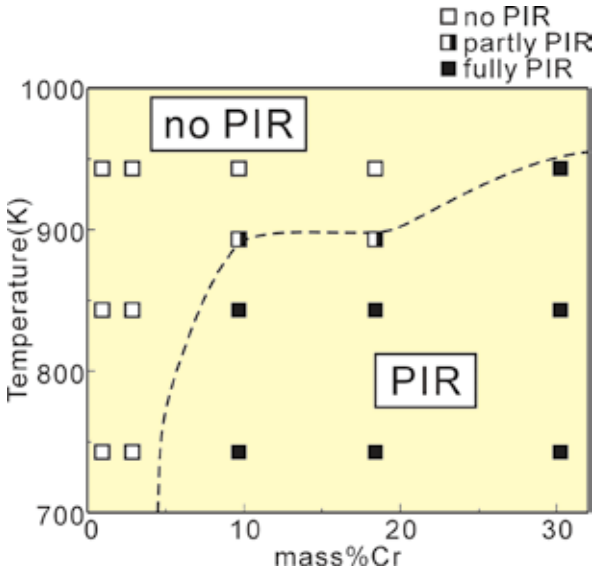

Fig. 2 Condition for PIR manifestation in nitriding of Fe-Cr alloys.

As shown above, PIR has been first clarified. This phenomenon has potential for being new surface modification method to obtain fine-grained structure composed of special grain boundary without any mechanical-deformation treatment.

References

[1] G. Miyamoto, A. Yonemoto, Y. Tanaka, T. Furuhara, T. Maki, Acta Mater., **54**, 4771 (2006)

[2] G. Miyamoto, A. Yonemoto , Y. Tanaka , T. Maki, T. Furuhara, ISIJ Inter., **47**, 1491 (2007)

Contact to
Tadashi Furuhara (High Purity Metallic Materials Division)
E-mail: Furuhara@imr.tohoku.ac.jp

Reduction of Dislocations in GaN films on AlN/sapphire Templates Using CrN Nanoislands

Significant reduction of threading dislocations was achieved in GaN films grown by hydride vapor phase epitaxy (HVPE) on AlN/sapphire templates by employing CrN nanoislands on AlN layer. We demonstrate that the density of threading dislocations can be efficiently reduced on AlN/sapphire templates. The CrN nanoislands play a key role in reducing threading dislocations by masking and bending the propagation of dislocations.

GaN based III-nitride materials and devices have been one of the hottest issues in compound semiconductor researches and related industries. Recently, studies on high-brightness deep UV LEDs or LDs emitting at wavelengths shorter than 360 nm have been receiving increasing interests [1]. In order to realize high-brightness deep-UV LEDs, the growth of high quality AlGaN/AlN templates is important, so several methods of high quality buffers such as AlN/AlGaN superlattices, AlGaN buffer, and GaN/AlN superlattices have been reported [2]. For the performance of GaN-based light emitters, the reduction of dislocation density is crucial for high internal quantum efficiency, since electron-hole pairs can recombine through non-radiative processes at dislocations. However, AlN films grown on sapphire substrates generally have high density of edge type threading dislocations, while small density of screw type threading dislocations. So there have been some efforts of reducing the dislocation density by special growth method such as epitaxial laterally overgrowth of GaN[3] (ELOG), which provides a dislocation density of ~10^6/cm^2. As reported by Mukai et al.[4], a UV GaN LED with 7 × 10^6/cm^2 dislocation density has about two fold higher output power than that with 1 × 10^{10}/cm^2 dislocation density.

In this study we report significant reduction of threading dislocations in GaN films grown by HVPE on AlN/sapphire templates by employing CrN nano-masks on the AlN. High quality GaN films with very small twist mosaics as well as small tilt mosaics have been grown on AlN/sapphire templates, though the AlN/sapphire templates have small tilt but very large twist mosaic. Fig. 1(a) shows a XRD θ-2θ scan of a Cr/AlN/sapphire sample after nitridation. We can see the (111) CrN peak in addition to the (0002) AlN, which indicates complete nitridation of the Cr layer into CrN. Fig. 1(b) shows a SEM micrograph a nitrided Cr layer, which consists of nano-sized triangular CrN hillocks with sizes ranging from 15 to 90nm.

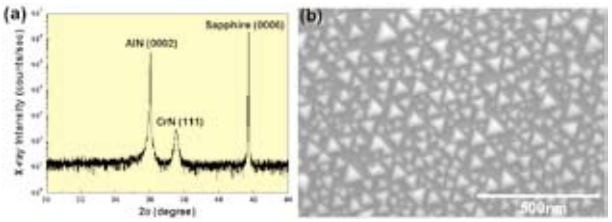

Fig. 1. XRD θ-2θ scan (a) and SEM microsgraph (b) of the Cr/AlN/Sapphire sample after the nitridation

In order to estimate dislocation densities, plan view TEM observations were performed, which are shown in Fig. 2(a) and (b) with the <0001> zone axis. Since there is a large lattice misfit of 17 % between GaN and sapphire, a GaN film grown on AlN templates without CrN contains majority of edge type dislocations which form low angle grain boundaries with a misangle of 0.7◦ as shown in Fig. 2(a). The estimated total dislocation density is 6.4 x10^9cm^{-2}. On the other hand, a GaN film grown with CrN buffer shows a significantly reduction of dislocation densities as shown in Fig. 2(b). The total dislocation is estimated to be 2.7 x10^8cm^{-2}. It should be noted that most of the dislocations observed in our samples were edge-type dislocations as shown in Fig. 2.

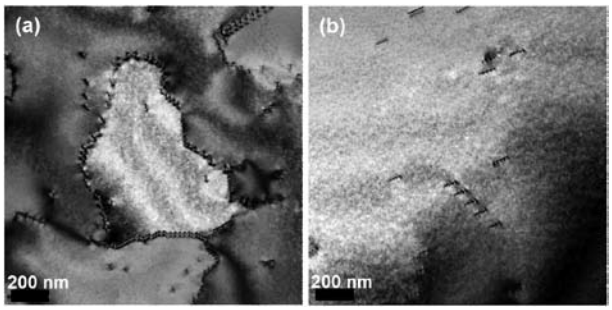

Fig. 2. Plan view bright-field TEM micrographs for the GaN films on the AlN/sapphire templates without (a) and with (b) the CrN.

In summary, we have demonstrated that the density of threading dislocations can be effciently reduced by employing CrN nano-masks on AlN/sapphire templates. The total dislocation density of a GaN film as evaluated by plan view TEM observation is reduced down to 2.7 x10^8cm^{-2}. The CrN nanoislands play a key role in reducing threading dislocations by masking the propagation of dislocations as well as by bending the dislocations. The studies on the effects of CrN nanoislands coverage i.e. the density of nanoislands will be the next topic for investigation.

References

[1] H.Hirayama, T.Yatabe, N. Noguchi, T.Ohashi, and N. Kamata, Appl. Phys. Lett. **91**, 071901 (2007)
[2] J. P. Zhang, A. Chitnis, V. Adivarahan, S. Wu, V.Madavilli, R. Pachipulusu, M. Shatalov, G. Simin, J. W. Yang, and M. Asif Khan, Appl. Phys. Lett. **81**, 4910 (2002).
[3] A. Usui, H. Sunakawa, A. Sakai, and A. A. Yamaguchi, Jpn. J. Appl. Phys., **36**, L899 (1997)
[4] T. Mukai, S. Nagahama, N. Iwasa, M. Senoh and T. Yamada, J. Phys.: Condens. Matter **13** 7089 (2001)

Contact to
Takafumi Yao (Electronics Materials Division)
e-mail: tyao@cir.tohoku.ac.jp

MOVPE Growth Mechanism of High-Quality N-polar GaN on C-Plane Sapphire

The MOVPE growth mechanism of the high-quality N-polar GaN with a smooth surface grown on c-plane sapphire has been clarified. The key issues cover sapphire nitridation, GaN buffer layer annealing, GaN growth temperature, and the supply of hydrogen and ammonia. These technologies will pave the way for industrial production of N-polar GaN-based devices.

During recent years, nitride semiconductors have been explored extensively, especially GaN and its related materials. Most of the nitride devices are fabricated with Ga-polar GaN grown on a c-plane sapphire substrate by MOVPE, which is a very good choice for large scale manufacturing. On the other hand, N-polar GaN is also a promising material giving a large flexibility to device design. However, the growth of N-polar GaN is difficult due to the low lateral growth speed, which leads to pyramidal surfaces. We have solved this problem and reported the first success in MOVPE growth of N-polar GaN with smooth surface [1]. The full width at half maximum of the X-ray diffraction spectra in ω-2θ and ω scan is 19 and 35 arcseconds, respectively, which is the smallest in the reported ones to our knowledge. Here we report the MOVPE growth mechanism of N-polar GaN [2].

GaN was grown using the two-step MOVPE growth technique with a low-temperature buffer layer on a (0001) sapphire substrate. Just before the growth, the sapphire substrate was treated with nitridation, followed by the growth of a 20 nm thick GaN buffer layer at 550°C using triethylgallium (TEG) and ammonia. The buffer layer was annealed at 1030°C for the crystallization. Finally, the 1~2μm thick GaN film was successively grown at 1020°C using trimethylgallium (TMG). To understand the growth mechanism, we investigated the effects of nitridation, annealing of a buffer-layer, high-temperature growth, and flow rates of ammonia and hydrogen.

Fig. 1 shows the surface morphologies of the GaN grown without and with nitridation of sapphire, observed by a differential interference contrast microscope. Pyramidal hilllocks dominate the GaN surface grown without nitridation (Fig. 1(a)), while a smooth surface was obtained with nitridation for 6 min. (Fig. 1(b)). This proper nitridation time is indispensable for acquiring N-polar GaN with a smooth surface, which is owing to a uniform N-polar AlN layer formation during the nitridation process.

From the comparison between as-grown and annealed GaN buffer-layers in observation of the atomic-force microscope (Fig. 2), the nuclei density is found to decrease from 11.4 $\times 10^8/cm^2$ to 4.8 $\times 10^8/cm^2$. Using this buffer layer, the grain in high-temperature grown GaN becomes large and as a result the dislocation density small. In addition, the anneal process changes spherical nuclei (Fig. 2(a)) to plain one (Fig. 2(b)) due to the etching of the GaN facets with high plane indexes in an ambient with hydrogen from the cracking of ammonia during annealing process. The plain nuclei are believed to enhance the step-flow growth of GaN grown at high temperature.

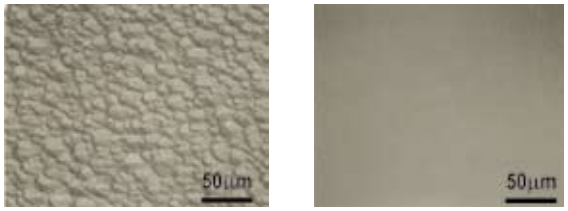

(a) without nitridation (b) with nitridation

Fig. 1 Surface morphology of GaN epitaxial layer.

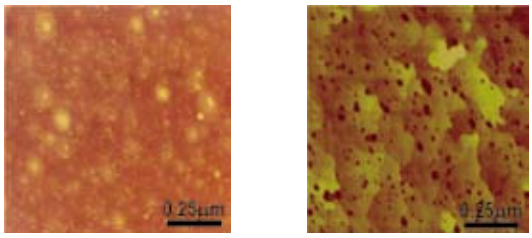

(a) as-grown (b) after annealing

Fig. 2 AFM image of GaN buffer.

In the high-temperature growth process, the growth temperature, the hydrogen and ammonia flow rates play important roles in GaN quality. The morphologies of the GaN grown at 1010°C, 1030°C, and 1050°C show a hillock, a flat, and a rough surface, respectively. At 1010°C, the migration length of Ga atoms is not enough for the step-flow during growth. Hence, 3-dimensional growth appears. At 1030°C, the migration length is enough and the step-flow occurs. At 1050°C, the nitrogen desorbs and GaN re-evaporation becomes strong. For the ammonia flow rate, an excess flow of ammonia gas forms the surface with hexagonal hillocks due to the poor migration of Ga-atoms, while its less flow can not supply enough nitrogen reactant and results in nitrogen vacancies generation. With increasing the hydrogen gas flow rate from 1.8slm to 7.5slm, the surface morphology was greatly improved as the 3-dimensional nuclei on the terrace were etched and the step-flow was enhanced.

These results are promising for establishing a standard for industrial fabrication of N-polar GaN with high quality grown by MOVPE. It can also be extended to grow N-polar InN [3]. Using N-polar growth technique, it is possible to improve the crystal quality of InN, thus making one step closer to implement an InN-based distributed-feedback laser for low-cost and high-capacity optical communications systems.

References

[1] Matsuoka, T. Mitate, H. Takahata, S. Mizuno, Y. Uchiyama, A. Sasaki, M. Yoshimoto, T. Ohnishi and M. Sumiya, phys. stat. sol. (b) **243**, 1446 (2006).
[2] N. Motegi, T. Kimura, M. Nakao, T. Toda, M. Hirata, Y. Liu and T. Matsuoka, ICNS7, X-7, Las Vegas, USA (2007).
[3] T. Matsuoka, Proceeding of SPIE, "Gallium Nitride Materials and Devices II", **6473**, 1 (2007)

Contact to
Takashi Matsuoka (Advanced Electronic Materials Research Division)
e-mail: matsuoka@imr.tohoku.ac.jp

Neutron Holography with Atomic Resolution

Atomic-resolution neutron holography was carried out utilizing the powder diffractometer in JRR-3M reactor. Spherically emitted neutrons around a $PdH_{0.78}$ single crystal produced by incoherent neutron-proton scattering, which formed a hologram, were efficiently collected using multi array ^3He detectors. In addition to the hologram data, strong undulation due to the elastic thermal scattering was observed. To exclude this effect, the sample was cooled to 100 K. The thermal scattering was properly removed.

Atomic resolution X-ray and electron holography has been developed in the last two decades.1-3) Since these techniques can visualize 3D local atomic arrangements around selected elements in solids, they have been attracted as local structural analysis of dopants and adsorbates. However, the photoelectron or X-ray holography has a disadvantage that they cannot apply to hydrogen system because hydrogen dose not emit any fluorescent X-rays and photoelectrons. In order to overcome this difficulty, neutron holography was proposed in 2001. First demonstration of the neutron holography was realized using a single crystal of simpsonite. They measured angular anisotropy of incoherently scattered neutrons from hydrogen nuclei, and reconstructed surrounded oxygen nucleus images. In 2004, Cser et al. applied this technique to a palladium hydride single crystal, and determined the location of hydrogen in the PdH. We also measured efficiently the neutron hologram of a palladium hydride single crystal using the powder diffrcatometer of HERMES in JRR-3M reactor, and found the thermal diffuse scattering effect in the measured hologram.4) However, strong undulation due to the elastic thermal scattering was observed. To exclude this effect, the thermal scattering pattern was calculated and subtracted from the measured data. From the resulting hologram data, neighboring Pd and H nuclei images were successfully reconstructed, as shown Fig. 1.

In this study, we used again a palladium hydride single crystal as the measured sample and evaluated the temperature dependence of the sample on the thermal diffuse scattering in the hologram. The sample dimension was 10 mm in a diameter and 5 mm in a thickness, and it was coated by Cu not to desorb the hydrogen gas. Wavelength of the neutron was 0.182 nm.

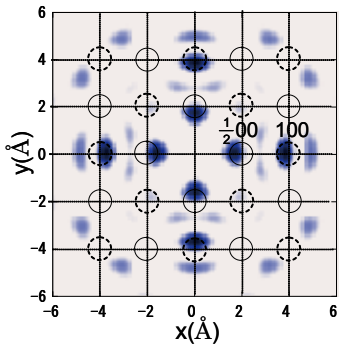

Fig. 1 Reconstructed real space-image of (001) plane around H in $PdH_{0.78}$.

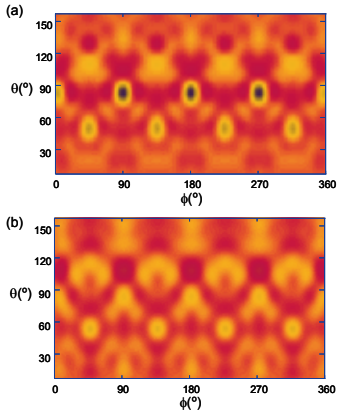

Fig. 2 Holograms of $PhH_{0.78}$ measured at room temperature (a) and 100 K (b), respectively.

Sample was rotated in the range of 0° ~ 359° with the step of 1°, where rotation axis was parallel to the incoming beam direction. Neutrons incoherently scattered by hydrogen nuclei in the sample were detected by HERMES 150 He^3 counters at each sample rotation angle. Polar angle of the measured hologram defined by the counter ranged from 7° to 157°. Dwelling time at each angle was 480 sec. The average neutron intensity at each pixel was about 500 counts. To reduce the effect of thermal diffuse scattering the cryostream cooler (Oxford: cryostream 70 series) was used for keeping the sample temperature at 100 K. Figures 2 (a) and (b) show the 2D angular distributions of the neutron intensities around the sample at room temperature and 100 K, respectively. The observed data were four-fold symmetrized using sample crystal symmetry in order to suppress statistical error, and then they were low-pass filtered. The displayed patterns exhibit strong spots reflecting the sample crystal symmetry, due to thermal diffuse scattering. However, the contrast of the pattern in Fig.2 (b) is weaker than that in Fig. 2 (a). Especially at polar angle of 80˚, the amplitude of the intensity change at room temperature was twice as much as that at 100 K. These results revealed that the effect of the thermal diffuse scattering effect was reduced by the sample cooling.

References

[1] K. Hayashi, Advances in Imaging and Electron Physics **140**, 119 (2006).
[2] K. Hayashi, T. Matsushita and E. Matsubara, Journal of the Physical Society of Japan **75**, 053601 (2006).
[3] K. Hayashi, T. Hayashi, T. Shishido, E. Matsubara, H. Makino ,T. Yao and T. Matsushita, Phys. Rev. B **76**, 014119 (2007).
[4] K. Hayashi, K. Ohoyama, S. Orimo, Y. Nakamori, H. Takahashi and K. Shibata, Japanese Journal of Applied Physics **47**, 2291 (2008).

Contact to
Kouichi Hayashi (Chemical Physics of Non-Crystalline Materials Division)
e-mail: khayashi@imr.tohoku.ac.jp

Biofunctional Porous Titanium Filled with Medical Polymer through Impregnated Monomer Polymerization Technique

A new process of polymer filling in pores of porous metallic materials was developed in this study. Such a polymer filling is expected to improve mechanical properties and biofunctionalities of porous metallic materials. Therefore, it was applied to polymethylmethacrylate (PMMA) filling in pores of porous pure titanium (pTi), and tensile strength and Young's modulus of pTi filled with PMMA were examined.

Low Young's modulus similar to that of human bone is one of the important properties for metallic biomaterials, because it is advantageous to inhibition of bone atrophy and absorption due to stress shielding. In order to obtain lower Young's modulus, one of the effective ways is to use porous materials. However, the mechanical properties of porous materials deteriorate with an increase in porosity. This deterioration may be attributable to the stress concentration near the pores of porous materials. Thus, the inhibition of the stress concentration due to filling up of the pores with certain materials is likely to improve their mechanical properties. In such a case, materials with low Young's modulus should be selected for filling in order to prevent an increase in Young's modulus. Furthermore, depending on the type of the filled materials, biofunctionalities, which are not intrinsically present in the metallic biomaterials, can be imparted to the porous materials in addition to the improvement of mechanical properties. In this study, the pores of porous pure titanium (pTi) were filled with a medical polymer, polymethylmethacrylate (PMMA), and then the effects of PMMA filling on the mechanical properties of pTi were investigated as a model case [1].

Fig. 1 shows the new process of polymer filling in pores of porous metallic materials developed in this study. A tensile specimen of pTi with the porosity of 22–50%, which is a porous sintered compact made of gas-atomized pure titanium powders, was soaked in monomer solution mixed with a polymerization initiator. After removing air babbles in pores under a reduced pressure, the impregnated monomer was polymerized by heating at a constant temperature under atmospheric pressure. Then, the extra part of PMMA was removed by mechanical machining.

The PMMA filling rate was evaluated by an image analysis technique, and a fairly high filling rate, greater than 98%, was obtained. Further, for one of the safety evaluations, the concentration of residual monomer eluted from PMMA into water at room temperature was analyzed by liquid chromatography. It was found that the residual monomer is suppressed by using relatively high concentration of polymerization initiator in monomer solution.

Fig. 2 shows the tensile strengths of both pTi and pTi filled with PMMA. They decrease with an increase in porosity. However, the tensile strengths of pTi filled with PMMA are higher than those of pTi in the high porosity range. This result indicates that the effect of the PMMA filling on the improvement of the tensile strength of pTi is likely to appear in the low tensile strength range of pTi. Moreover, Young's moduli of pTi and pTi filled with PMMA were measured using the stress–strain curve obtained by tensile test. It was observed that the PMMA filling hardly affected Young's modulus of pTi because Young's modulus of PMMA is lower than that of pTi.

The process of polymer filling in pores of porous metallic materials developed in this study is likely to be applied to different polymers other than PMMA. By selecting a proper polymer, biofunctionalities are able to be provided to porous metallic materials.

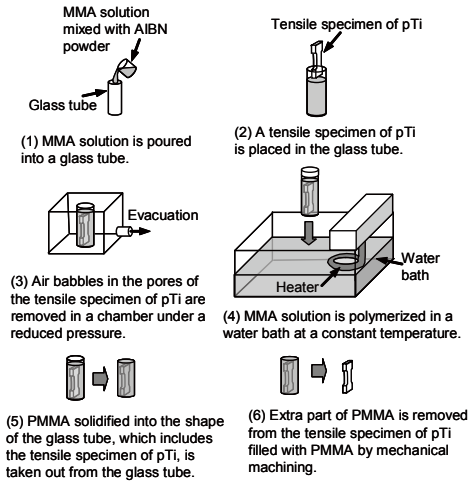

Fig. 1 Schematic drawing of process of PMMA filling in pores of porous pure titanium.

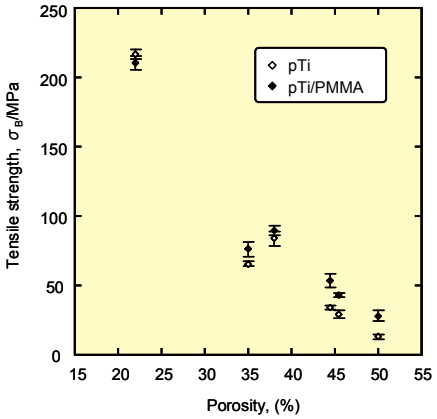

Fig. 2 Tensile strengths of pTi and pTi filled with PMMA as a function of porosity.

Reference

[1] M. Nakai, M. Niinomi, T. Akahori, Y. Shinozaki, H. Toda, S. Itsuno, N. Haraguchi, Y. Itoh, T. Ogasawara and T. Onishi, Proc. Int. Conf. on Advanced Technology in Experimental Mechanics 2007 (ATEM'07), CD-ROM, (2007).

Contact to
Mitsuo Niinomi (Biomaterials Science Division)
e-mail: niinomi@imr.tohoku.ac.jp

Fundamental Aspects of Bulk Metallic Glasses

This article reports our recent research results of fundamental aspects of bulk metallic glasses (BMGs) in terms of (1) a newly developed molecular dynamics simulation method to analyze the formation of liquid phase and (2) mechanisms of the stress-overshoot phenomenon and non-Newtonian viscous flow around T_g

A computational method using molecular dynamics simulations to create a noncrystalline structure from a crystalline compound related to metallic glass has been proposed based on the idea that groups of atoms in a compound can be treated as hypothetical clusters [1]. This method was hinted by an illustration in an old literature in 1960 [2] as shown in Fig. 1(a), showing that a C_6C_{23} crystalline structure is drawn as an ensemble of clusters and atoms. When we saw Fig. 1(a) at the first time, we hit on an idea that "What would be the structure if the clusters are allowed random rotations around the center of gravity?", which state is illustrated in Fig. 1(b). The computation in terms of pair-distribution revealed that atomic arrangements expressed by Fig. 1(b) exhibit a sharp peaks corresponding to a crystalline phase at an interatomic distance shorter than 1 nm. However, the atomic arrangements shown in Fig. 1(b) lose long-range periodicity at a long interatomic distance of about 1 nm, which is a characteristic of a crystalline phase. Hence, we understood that the atomic arrangements shown in Fig. 1 (b) can be an intermediate state to transform from a crystalline state (Fig. 1 (a)) to a liquid phase. After that we confirmed that atomic arrangements similar to a liquid phase are obtainable by structural relaxation to a state illustrated in Fig. 1 (b). The following conclusions have been achieved by the analysis [1]. A computational method to create noncrystalline structure directly from a crystalline structure, which is related to metallic glasses, has been proposed. The basis of this method is that it handles groups of atoms as hypothetical cluster. To verify its applicability, this scheme was applied to a C_6C_{23} structure type, which revealed the similarity in the local atomic arrangements between the computationally relaxed C_6C_{23} structure and the liquid phase when the clusters are permitted to rotate before the C_6C_{23} structure relaxes. The C_6Cr_{23} structure can be regarded as an ensemble of atoms and clusters, which leads to the C_6Cr_{23} structure to be equivalent to Cu_2AlMn structure type in bcc derivative structure family. The noncrystalline forming-ability of the C_6Cr_{23} structure is due to the low packing factor of the C_6C_{23} structure in the bcc derivative structure family, which provides extra freedom by permitting random cluster-rotations. The significance of the present scheme is that clusters are used to analyze the local atomic arrangements in a metallic system and that a noncrystalline structure is produced from an actual alloy compound with the aid of computer calculations.

One of the most attractive properties of bulk metallic glass (BMG), whose fracture strength at the ambient temperature is usually in GPa order, is its excellent workability driven by low

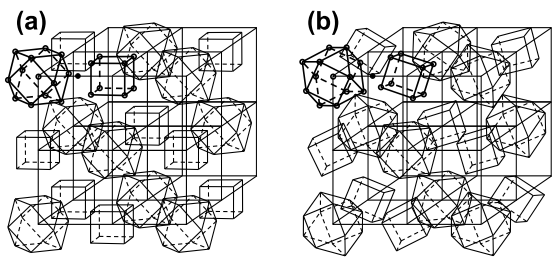

Fig. 1 Schematic illustrations showing (a) C_6C_{23} crystalilne structure drawn as an ensemble of clusters and atoms, and (b) a state where hypothetical cluster rotations around the center of gravity were allowed to the crystalline structure.

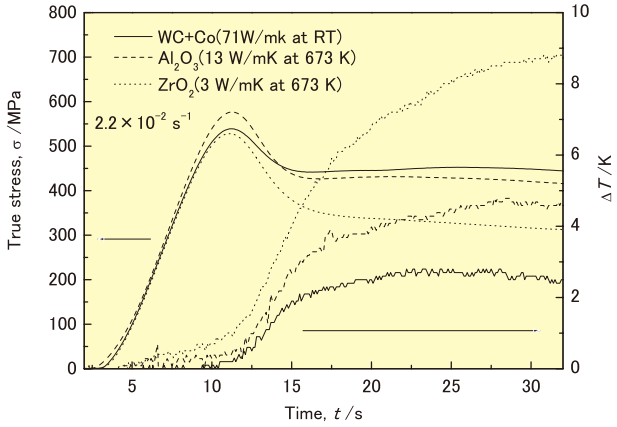

Fig. 2 Dependence of true stress and temperature rise of sample due to the viscous frictional loss at a strain rate of 2.2×10^{-2} s^{-1} on thermal conductivity of the die-plates. The initial testing temperature was set at 690 K.

applied stress in kPa~MPa order at the supercooled liquid state (SCL). We can deform BMGs easily for more than 10,000 % of elongation and imprint nano-sized patterns on the surface of BMGs very precisely [3]. These can be performed with the homogeneous viscous flow. The stress-overshoot phenomenon is known to be a nonlinear viscoelastic behavior, which brings the steady-state homogeneous non-Newtonian viscous flow around the glass transition temperature (T_g). Therefore, it is important to understand the mechanism of the stress-overshoot phenomenon. *In-situ* observations of the stress-overshoot phenomenon and enthalpy evolution related to the structural relaxation driven by the stress as well as temperature have been carried out in a Zr-based BMG via direct measurements of stress as well as sample temperature under compressive constant ram-velocity deformations [4]. The results indicate that the structural relaxation related to the softening phenomenon is triggered by the applied stress, and the increase in the sample temperature caused by the viscous frictional loss of the non-Newtonian flow also contributes to the softening phenomenon of the sample. This indicates that sample temperature, thus, viscosity during the working is affected by the heat conductivity of the surrounding materials, i.e., die, punch for the shaping or mold for the imprinting. Figure 2 fairly demonstrates the dependence of the steady -state flow stress observed after the stress-overshoot phenomenon in the Zr-based BMG on the die materials with different heat conductivity, i.e., WC/Co (71 W/m K), alumina (13 W/m K) and ZrO_2 (3 W/m K). This is telling us that a die (or mold) with lower heat conductivity is more appropriate for shaping (or imprinting) BMGs.

References

[1] A. Takeuchi and A. Inoue, Intermetallics, **16**, 283 (2008)
[2] W. Hume-Rothery and G.V. Raynor, "The structure of metals and alloys", The Institute of Metals, Richard Clay and Company, U.K., 1962.
[3] Y. Saotome, K. Imai, S. Shioda, S. Shimizu, T. Zhang and A. Inoue, Intermetallics, **10**, 1241 (2002).
[4] H. Kato, A. Inoue and H. S. Chen, J. Non-cryst. Solid, **353**, 3764 (2007).

Contact to
Hidemi Kato (Non-Equilibrium Materials Division)
e-mail: nano2000@imr.tohoku.ac.jp

Giant Spin Hall Effect in Gold with a Perpendicular Spin Injector

In the field of "spin-electronics", which takes advantage of the freedom of spins and provides electronic devices with multi-functionality, the generation and detection of the flow of spins (so-called "spin current") are keys. Recently, spin Hall effects (SHEs) in nonmagnetic materials have attracted much attention because this enables us to generate or detect the spin current without a ferromagnetic material. This new type of Hall effect opens the way for the further advances of spin-electronic devices.

The SHE is generally considered to be the anomalous Hall effect (AHE) in a nonmagnetic metal or semiconductor. The most distinguished point of the SHE is that it does not require ferromagnetic order. When an unpolarized charge current flows in a nonmagnetic material having a large spin-orbit coupling parameter, the electrons are scattered in the transverse direction. The scattered directions are opposite between the up- and down-spin electrons (Fig. 1 (a)). This means that the flow of spins, *i.e.*, a spin current appears, which is called the direct SHE (DSHE). On the other hand, a spin current induces the transverse charge current (Fig. 1 (b)), which is called the inverse SHE (ISHE). The SHE enables the conversion between charge and spin currents in nonmagnetic materials. Although it fascinates us to incorporate this effect into the applications, the complicated device structures or the sophisticated measurement techniques were required to detect the SHE in previous studies. In addition, the small magnitudes of spin Hall signals has limited the possibility of device applications of SHE.

We developed a multi-terminal device showing a "giant SHE" at room temperature [1]. A present multi-terminal device has a nano-sized Au Hall cross and a FePt perpendicular spin injector, which is schematically shown in Fig. 1 (c). Perpendicularly magnetized FePt generates or detects perpendicularly polarized spin current without external magnetic field, which simplifies the device structure. A great advantage of the present multi-terminal device is that three kinds of Hall effects, *i.e.* DSHE, ISHE, and local Hall effect (LHE) are measured in the same device. We employed

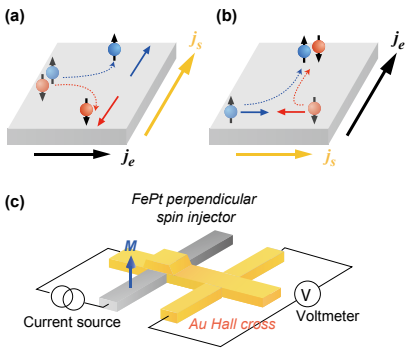

Fig. 1 Schematic illustrations of the concepts of (a) direct spin Hall effect and (b) inverse spin Hall effect. J_e and J_s are the charge current and the spin current, respectively. (c) A schematic illustration of the multi-terminal device consisting of the Au Hall cross and the FePt perpendicular spin injector.

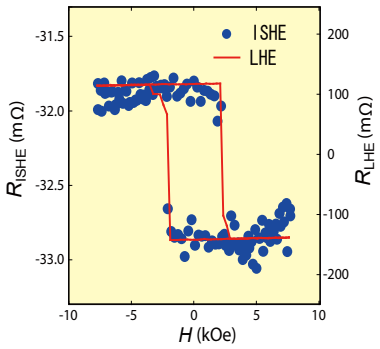

Fig. 2 Resistance of the inverse spin Hall effect (R_{ISHE}) as a function of external magnetic field (H) measured at room temperature. For comparison, the resistance of the local Hall effect (R_{LHE}) is also shown (red lines)

a non-local spin injection technique to detect DSHE and ISHE. In the case of the ISHE, a spin-polarized electric current is injected from FePt to Au, and the spin current flows in Au due to the spin accumulation. Then, the non-local Hall voltage induced by the ISHE is detected by the Au Hall cross. For the DSHE, on the other hand, the FePt spin injector act as a spin detector measuring the spin-dependent electrochemical potential at the FePt/Au interface. When an electric current flows in the Au Hall cross, the spin current is generated by the DSHE, and the generated spin current is detected by the FePt spin injector. An important point is that the SHE is detected even at zero external magnetic field owing to the perpendicular magnetization of FePt.

Figure 2 shows the non-local Hall resistance in the ISHE geometry (R_{ISHE}) as a function of external magnetic field (H). A clear hysteretic transition of R_{ISHE} is observed, and the shape of its hysteresis loop was the same as that of the LHE (red line), which means that the hysteresis loop of RISHE reflects the magnetization reversal of FePt. A similar hysteresis of the non-local resistance was also observed in the DSHE geometry. From the resistance change of the SHE, the spin Hall angle, which is the ratio of the spin Hall conductivity to the electric conductivity (σ_{SH}/σ), was calculated to be 0.113. This large spin Hall angle in Au is interpreted by the skew scattering mechanism. The maximum resistance change (ΔR_{ISHE}) at room temperature is obtained to be 2.9 mΩ for the device with d = 70 nm, which is significantly larger than those in previous studies. We believe that the large spin Hall signal opens the way for the further development of spin-electronic devices.

Reference

[1] T. Seki, Y. Hasegawa, S. Mitani, S. Takahashi, H. Imamura, S. Maekawa, J. Nitta and K. Takanashi, Nature Mater. **7**, 125 (2008).

Contact to
Koki Takanashi (Magnetic Materials Division)
e-mail: koki@imr.tohoku.ac.jp

Low-Temperature and High-Speed Deposition of α-alumina Coatings by Laser Chemical Vapor Deposition

α-Al_2O_3 (α-alumina) coating is of great interest as ware- and heat- resistant coating on cutting tools due to their high hardness and chemical stability at high temperatures. Conventional thermal chemical vapor deposition (CVD) has been commercially applied on WC-Co-base cutting tools. In order to enable to coat α-alumina on TiNi-base cermets, the decrease of deposition temperature is essential. In this study,α-Al_2O_3 coating succeeded at a low deposition temperature by developing laser chemical CVD.

Cemented carbides such as WC-Co have been widely used as cutting tool material. Nowadays, heat-resistant coated cemented carbide cutting tools are developing for high-speed cutting and dry cutting without cooling lubricants. α-Al_2O_3 coating is crucial to commercialize cermet-based cutting tools such as TiN-Ni. However, no study has succeeded to coat α-Al_2O_3 on cermet-based cutting tools due to too high deposition temperature causing outward diffusion of Ni.

Chemical vapor deposition (CVD) can produce high quality crystalline Al_2O_3 coatings. However, a conventional thermal CVD technique requires high deposition temperature over 1300 K to obtain α-Al_2O_3. The deposition rate of α-Al_2O_3 by conventional thermal CVD is too low around several μm/h. A thickness of coating should be 20 to 50 μm to elongate the life-time, and then a high deposition rate has been demanded.

Last year, the Ministry of Economy, Trade and Industry (METI) has started "Development of alternative materials to rare metal project", where W (tungsten) has nominated as one of four rare metals. A new hard material for cutting tools with a small amount or without W should be developed. We are going to conduct the project to produce high-performance thick Al_2O_3 coating on cutting tools.

We have invented a new laser CVD process[1-3] to fabricate α-Al_2O_3 coating at a low deposition temperature and a high deposition rate. We have been systematically investigating the optimum deposition conditions to obtain high quality α-Al_2O_3 coating.

An experimental procedure is as follows: A substrate is placed on a heating stage in the CVD chamber and pre-heated. Tri-acetyiacetonate aluminum ($Al(acac)_3$) precursor vapor and O_2 gas are supplied to the substrate through a double nozzle, and Nd:YAG laser (wavelength:1063 nm, laser power(P_L): 0-250 W) is irradiated to the whole substrate surface by expanding a laser beam. The substrate temperature during deposition (T_{dep}) is measured by a thermocouple. The chemical reaction between precursor vapor and O_2 gas is significantly enhanced by plasma formed around the substrate.

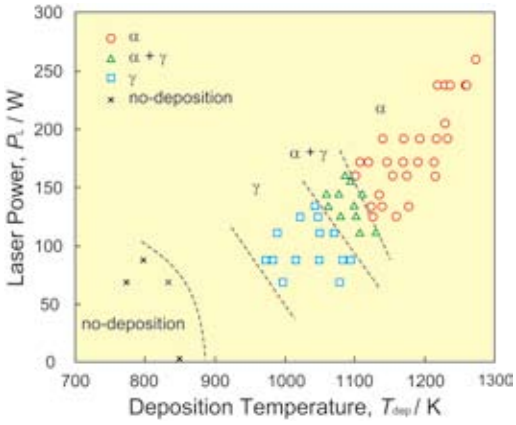

Fig. 1 Effects of T_{dep} and P_L on crystalline phases

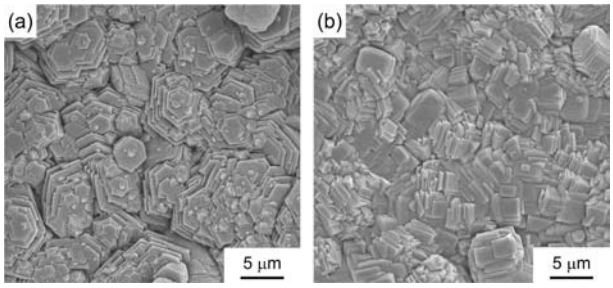

Fig. 2 Surface morphologies of α-Al_2O_3 prepared at (a) P_L = 172 W, T_{vap} = 443 K and (b) P_L = 192 W, T_{vap} = 413 K

Fig.1 shows the effects of T_{dep} and P_L on crystalline phases of Al_2O_3 coatings. Crystalline phases have changed from γ to γ+α to α with increasing T_{dep} and P_L. The lowest T_{dep} for α-Al_2O_3 is 1122 K at P_L = 160W, which is 150 K lower than that of commercial thermal CVD. The deposition rates of Al_2O_3 have ranged from 250 to 320μm/h at a precursor vaporization temperature of 443 K, and are several 10s to several 100s times higher than those of thermal CVD.

The crystalline orientation of α-Al_2O_3 has been controlled by deposition conditions. The (300), (104), (006) and non-oriented α-Al_2O_3 coatings have been fabricated. The microstructures of α-Al_2O_3 coating have well correlated with the crystalline orientations. Fig.2 demonstrates typical surface morphologies of α-Al_2O_3 coating with different crystalline orientations. Fig.2 (a) shows a surface SEM image of (006) oriented α-Al_2O_3, in which hexagonal plate-like crystal grains can be observed, while Fig.2 (b) shows (300) oriented rectangular morphology.

References

[1] T. Goto, R. Banal, T. Kimura, Surf. Coat. Technol.,**201**, 5776 (2007).
[2] T. Goto, T. Kimura, Thin Solid Films, **515**, 46 (2006),.
[3] T. Goto, T. Kimura, Key Engineering Materials, **317-318**, 495 (2006).

Contact to
Takashi Goto (Multi-functional Materials Science Division)
e-mail: goto@imr.tohoku.ac.jp

Development of Co Based and Ti Based Alloys for Highly-functional Structural Materials

New type of biomedical Co-Cr-Mo-N alloy and structural α' type Ti alloy with excellent ductility are proposed in these researches. In these developed alloys, high-function is achieved by controlling the alloying element, content, microstructure and thermo-mechanical condition.

Co-Cr-Mo alloys are one of the most useful alloys for biomedical applications such as dental and orthopedic implants. However, cast Co-Cr-Mo alloys exhibit low ductility due to the formation of shrinkage porosity, interdendritic segregation, and intermetallic inclusion of σ at the grain boundaries. Stabilizing the γ phase (F.C.C.) is thought to be effective for improving the low ductility in cast Co-Cr-Mo alloys. Ni, C and N are recognized to stabilize the γ phase in Co alloys. Among these γ stabilizing elements, the effect of N addition into Co-Cr-Mo alloy on microstructure and mechanical properties is not well understood. Therefore, this work aims at examining these properties of N-added Co-Cr-Mo alloys with various Cr contents.

Co-(29~34) mass%Cr-(5~5.8) mass%Mo-(0.01~0.6) mass%N alloys are prepared using a high-frequency vacuum induction furnace in this study. Since compositional changes before and after the casting are negligible, therefore the composition will be denoted hereafter by nominal composition abbreviated as (29~34) Cr. After casting, no apparent change in dendritic structure among alloys of (29~34) Cr can be seen. Concerning the evolution in phase constituent, N addition into Co-Cr-Mo alloys stabilizes γ phase without precipitation of brittle σ phase even in the enrichment in Cr content from 29 to 34 mass%. Accompanying with the increase in Cr content, the solubility of N into γ phase increases, thereby, resulting in the significant improvement in mechanical properties especially for ductility with increasing the (Cr+N) content (Figure 1)[1].

Thus this study reveals that the Ni-free Co-Cr-Mo alloys with enriched Cr content up to 34 mass%, modified by N addition, are suitable as materials for artificial hip and knee joints and dental implants that are produced on the basis of the casting process such as investment casting.

And recently, we have presented a new type of Ti alloys with low Young's modulus, high strength and high ductility for structural applications such as springs, screws and flexible fibers. The developed alloys are composed of fully α' martensite (H.C.P.) and hence their microstructure is stable during heating up to 600K. This thermal stability of α' Ti alloy is advantageous for the structural applications as compared with conventional β type Ti alloys. However, the characteristic causing the high ductility in α' alloy as compared with (α+β) alloy is uncertain, therefore, this work focuses on the examination of the deformation behavior in new type α' Ti alloy.

Acicular α' martensitic structure of quenched Ti alloy evolves by cold rolling into extremely refined dislocation-cell structure with an average grain size of 60nm, accompanied by the development of rolling texture in which the basal plane is tilted ±40~50 degrees for nominal direction(ND) to transverse direction (TD), and rolling direction (RD) is close to <$\bar{1}$ 100> orientation [2][3]. Fracture mode after tensile test is dependent on the testing orientation from RD to TD (Figure 2). Supposing that the quasi-cleavage plane corresponds to the primary active slip plane, fracture manner of cold rolled α' Ti alloy can be reasonably explained in terms of the primary activation of <*a*+*c*> dislocation[2]. This result implies the excellent ductility in α' alloy as compared with (α+β) alloy is caused by the activation of <*a*+*c*> slip. Also, this deformation behavior in α' Ti alloy suggests the possibility of the material production (for sheet, bar and wire of Ti alloy) under cold working (so called α' processing).

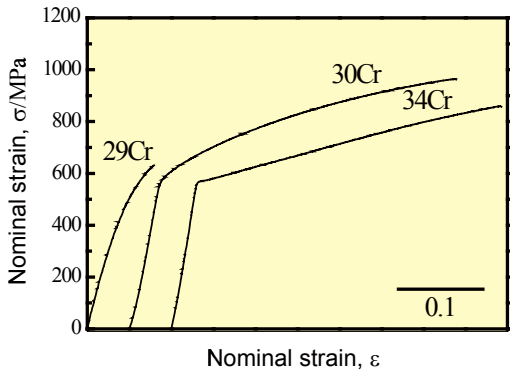

Fig.1 Stress strain curves of cast Co-Cr-Mo-N alloys.

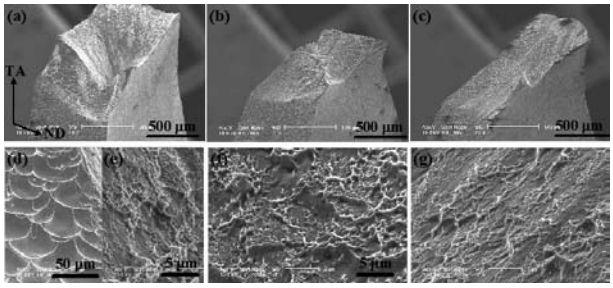

Fig.2 Fractographs of cold rolled (Ti-8%V)-4%Sn alloy after tensile test. Testing direction: (a)(d, e) RD, (b)(f) 45°from RD, (c)(g) TD.

References

[1] S. H. Lee, N. Nomura, A. Chiba, Mater. Trans. **49**, 260 (2008).

[2] H. Matsumoto, A. Chiba, S. Hanada, Mate. Sci. Eng. A **486**, 503 (2008).

[3] H. Matsumoto, S. Watanabe, S.Hanada, Mate. Sci. Eng. A **448**, 39 (2007).

Contact to
Akihiko Chiba (Deformation Processing Devision)
e-mail: a.chiba@imr.tohoku.ac.jp

Quenched Structure in Tetragonal-Monoclinic Phase Transition of Non-doped ZrO_2 Nano-Layer

Although zirconia (ZrO_2) has attractive properties for high-k gate dielectrics and buffer layers in semiconductor devices, its application is not possible due to the tetragonal-monoclinic (t-m) phase transition. In the present study, it was elucidated that the phase transition was quenched in the ultra-thin ZrO_2 layer deposited on a Si wafer. The layer had an atomically sharp coherent phase boundary, flat surface and interface. This means that a way to circumvent the harmful t-m phase transition in ZrO_2 has been found.

Yttria stabilized zirconia (YSZ) is an attractive material as a buffer layer for metal-insulator-semiconductor (MIS)-type Si devices such as ferroelectric gate transistors and superconductive devices. One of the critical issues concerning YSZ is the instability of the threshold voltage of an MIS-field effect transistor (MIS-FET) due to the large hysteresis of their capacitance-voltage (C-V) characteristics. The hysteresis is ascribed to mobile ions or polarization caused by oxygen vacancies and related defects [1]. Furthermore, the diffusion of doping elements into the Si substrate increases interface-trapped charges. Use of pure ZrO_2 is effective to avoid the C-V hysteresis and interface-trapped charges attributable to the doped elements such as Y. However, ZrO_2 has a monoclinic phase with large spontaneous strain, thus resulting in a complicated domain (twin) structure with large roughness at surfaces and interfaces [2]. Therefore, monoclinic ZrO_2 itself cannot be used for the gate dielectrics and buffer layers. We succeeded in elucidating (1) the film morphologies of a normal monoclinic phase ZrO_2 thin film, and (2) the size effect in the film thickness that controls the tetragonal-monoclinic phase transition of ZrO_2 [2].

Un-doped ZrO_2 films were deposited on a Si(001) wafer with thin SiO_2 layers by the Pulsed-Laser Deposition (PLD) technique. The nanostructure and interface of the films were investigated using high-resolution transmission electron microscopy (TEM). Figure 1 (a) shows a plan-view image of the 17-nm ZrO_2 film, where 90° and 180° domain structures are separated, respectively, with (110) and (100) planes. Figure 1(b) shows a plan-view image with diffractograms of each area of the image of 3-nm ZrO_2 film, where the precipitate (B,C) exists in the matrix (A). Diffractograms, which are two-dimensional Fourier transformed patterns of regions A, B, and C, indicate that the matrix is the tetragonal or cubic phase and that the precipitate is the monoclinic phase. Figure 2 (a) shows a cross-sectional image of the film observed in the [010] direction of 17-nm ZrO_2 film. The monoclinic phase has a coherent interface with tetragonal matrix. The (002) planes are tilted about 8.1° from the Si surface in the inclined area. The interface roughness and the surface roughness are large due to the lattice tilt of the ZrO_2 buffer layer, which causes the local misorientation of the oxide layers grown on the buffer layer. It is also unsuitable for application in high-k gate dielectrics. Figure 2 (b) shows a cross-sectional image of the 3-nm ZrO_2 ultra-thin film projected in the $[\bar{1}10]$ direction. The projected lattice image of the ZrO_2 layer has orthogonal symmetry, and the lattice parameter in the out-of plane direction is larger than that of the in-plane direction. Therefore, 3-nm ZrO_2 ultra-thin film is mainly composed of the tetragonal phase with nano-scale precipitates of the monoclinic phase. These results indicate that the tetragonal-monoclinic phase transition was quenched due to a type of size effect in the direction of film thickness. Two possible reasons are considered: the increased contribution of surface stress induced in the ultra-thin film compared with thicker films, and compressive stress induced by the dilative phase transition from the tetragonal to the monoclinic phase.

In summary, we found ultra-thin ZrO_2 film with a thickness of only 3-nm is adequate for buffer layers and gate dielectrics. The present results show that an ultra-thin film can overcome the structural issue of the monoclinic phase ZrO_2 thin films, which can contribute to solving the electrical issue of a conventional YSZ buffer layer and gate dielectrics resulting from dopant cations and oxygen vacancies.

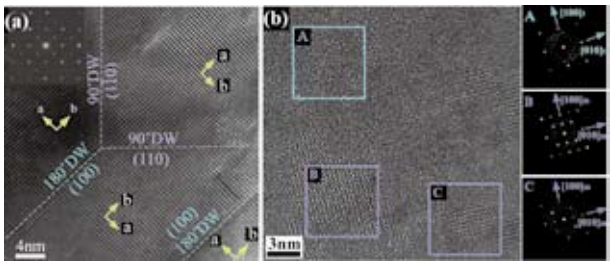

Figure 1 Plan-view image of ZrO_2 film of (a) 17nmn and (b) 3nm in thickness.

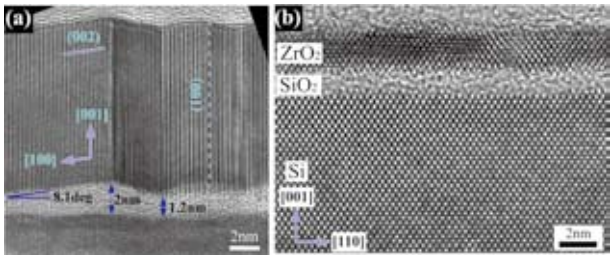

Figure 2 Cross-sectional image of ZrO_2 film of (a) 17nmn and (b) 3nm in thickness.

Referrences

[1] T. Kiguchi, N. Wakiya, K. Shinozaki, N. Mizutani, Mat. Res. Soc. Symp. Proc **748**, 171 (2003).

[2] T. Kiguchi, N. Wakiya, J. Tanaka, and K. Shinozaki, Mater. Sci. Eng. B **148**, 30 (2008).

Contact to
Takanori Kiguchi (Advanced Analysis of Materials Division)
e-mail: tkiguchi@imr.tohoku.ac.jp

Coulomb Oscillation of a Proton in a Ni-Nb-Zr-H Glassy Alloy with Multiple Junctions

Electric current-induced voltage oscillation at 500-560 kHz was observed in the current-voltage curves of nanoscopic size (~0.9-nm) tunnel junctions arranged in a low-capacitance (~1aF), multiple-junction configuration of $(Ni_{42}Nb_{28}Zr_{30})_{100-x}H_x$ (5.2≤x≤15.2) glassy alloys in the temperature range of 205 K to 6 K. This behaviour appeared to be derived from Coulomb oscillation resulting from the tunnelling of individual protons charging and discharging the vacancy capacitance of Zr-H-□-H-Zr atomic bond arrays among Zr-tetrahedral clusters, where □ is the vacancy barrier, termed the free volume, in the glassy alloys [1].

Following the discovery of the single-electron transistor[2], many research groups have studied the 'Coulomb blockade' effect, in which charge transport through the device occurs in an electron-by-electron manner at low temperatures. This means that a single electron on a metallic island can block the flow of another electron if the charging energy of the island greatly exceeds the thermal energy *kT*. The Coulomb blockade effects in mesoscopic systems with nanostructures show nonlinear responses to the externally connected macroscopic system.

In the present report, in the light of new developments, we consider the possibility of a nonlinear proton mode, using a glassy alloy that contains hydrogen. Glassy alloys are peculiar metallic alloys in that they lack the short-, medium-or long-range cyclic order of crystalline alloys, on the nanoscale. Therefore, the metallic glass is considered to be a macroscopic material with a mesoscopic system that consists of nanostructures.

For metallic glass that consists of antinomic affinity Zr and anti-affinity Ni elements for hydrogen[3], a melt-spun flexible amorphous $Ni_{42}Nb_{28}Zr_{30}$ membrane with excellent hydrogen permeability was selected. The $Ni_{42}Nb_{28}Zr_{30}$ material is a typical metal-metal type alloy that consists of familiar transition elements. Our interest lies in investigating the temperature-dependent hydrogen effect of electric conduction of the $(Ni_{42}Nb_{28}Zr_{30})_{100-x}H_x$ glassy alloys in terms of Coulomb oscillation. However, these are no previous reports on this subject for glassy alloys with hydrogen.

The electrical resistances of $(Ni_{42}Nb_{28}Zr_{30})_{1-x}H_x$ (x=0~0.22) alloys under 1 mA DC current with positive sign were measured during cooling and heating runs. We observed the abnormal resistivity variations (Fig.1). The abnormal variations in the two runs occurred at restricted hydrogen concentrations of 5.2 to 15.2 at% H and within the temperature range of 200 K to 6 K (insert, Fig.1). The wave pattern and power spectrum showed an AC saw wave with voltage oscillation of 560 kHz. The desorbed hydrogen from specimens during DC operation could not be measured by a quadrupole mass spectrometry. Thus it is clear that this abnormal behaviour is a DC current-induced AC oscillation, which is associated with the quantum mechanism of solute hydrogen. This oscillation is suggested to arise from sequential quantised charging of the sample.

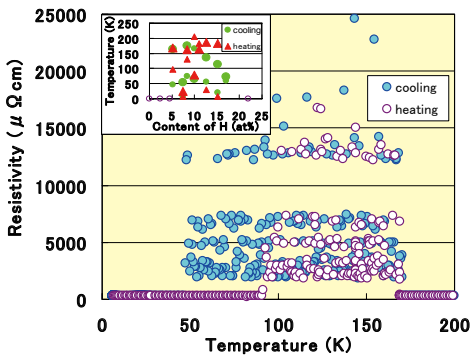

Fig.1 Abnormal resistivity of the $(Ni_{42}Nb_{28}Zr_{30})_{94.8}H_{5.2}$ alloy. Insert: Voltage variation with temperature and hydrogen content.

Based on the present results, it is possible that the abnormal behaviour of interest is a Coulomb oscillation that arises from the tunnelling of an individual proton charging and discharging the capacitance, thereby producing discrete voltage jumps with 2nd -3rd order of *e*/*C* in Ni-Nb-Zr-H glassy alloys. From the 4-coordination sites that are surrounded in a tetrahedral pattern by four Zr atoms, we propose a schematic representation of a microscopic junction between the Zr-tetrahedral clusters in the Ni-Nb-Zr-H glassy alloy (Fig.2a). In metallic glasses, an atomic Zr-H-□-H-Zr array corresponds to a single Coulomb blockade tunnelling junction, where □ is a vacancy barrier with electrostatic capacitance C.

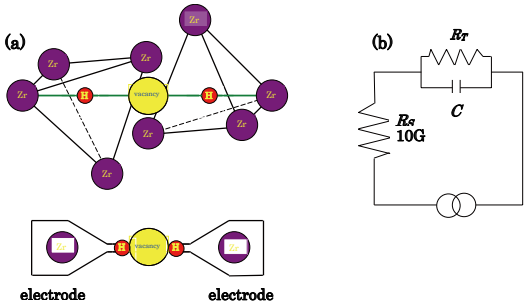

Fig.2 Hydrogen tunnelling model (a) for two tetrahedral clusters and blocking oscillation circuit (b). The solid circles represent is Zr atoms (purple), hydrogen atoms (red), vacancies (yellow).

References

[1] M.Fukuhara, A.Kawashima, S.Yamaura and A.Inoue, Appl.Phys.Lett., **90**, 203111 (2007).

[2] M.A.Kastner,P.F.Kwasnick and J.C.Licini, Phys.Rev. **B**,**36**,8015(1987).

[3] M.Fukuhara, A.Kawashima, S.Yamaura and A.Inoue, Phys.Stat. Sol. (RRL), **1**,R50 (2007).

Contact to
Mikio Fukuhara (Research and Development Project on Advanced Metallic Glass, Inorganic Materials and Joining Technology)
e-mail: fukuhara@imr.tohoku.ac.jp

Nanowire and Nanotube Made of Metallic Glass

Metallic glass nanowires were spontaneously created on the fracture surfaces that were produced by a conventional mechanical test. The presence of the nanowires is directly related to the one-dimensional meniscus configuration with a small viscosity at high temperatures and to the wide supercooled liquid region of the metallic glass. The electron microscopic observations demonstrate the diameters, the lengths, and the amorphous structural states, and the energy dispersive X-ray reveals the chemical components. In addition, we found that round ridges are constructed from nanotubes. The finding of amorphous nanostructures provides not only fundamental understanding of fracture processes but also give a new insight into nano-engineering constructions [1].

Bulk metallic glass (BMG) received attention because they offer unique mechanical properties such as ultrahigh strength, high hardness, and large elastic strain due to the absence of crystal slip. There have been extensive studies regarding the mechanical behavior of the BMGs that is associated with the nanoscale structural evolution including the dynamic crack propagation, the nano-crystallization along shear bands, and the microstructure formation. However, far less attention has been paid for the formation of the metallic glass nanostructures though they are expected to inherit the superior mechanical properties. Nevertheless, the metallic amorphous or glassy nanowires have not been achieved experimentally, in particular, formed by mechanical processes during fracture.

Figure 1(a) represents the SEM image of the fracture surface of the $Zr_{50}Cu_{40}Al_{10}$ BMG. The morphology like cellular "vein pattern" consists of the network of round ridges. The red arrows indicate nanostructures that can be recognized even in the low magnification SEM image. The image in Fig. 1(b) shows a nanowire having 100 nm in diameter that has droplets at each end. To identify the structural phases of nanowires, we employed the FIB technique and a vein texture was sliced for TEM observations. To avoid excessive milling of the nanowire, a $W(CO)_6$ gas was exposed to the surface and the side walls of the sample was milled until the thickness of ~0.1 μm, as depicted in Fig. 1(c). Figure 1(d) is the bright-field TEM image showing the cross section of the nanowire that has 240 nm in diameter. The inset shows the electron diffraction pattern that is obtained from the center of the nanowire. The diffused pattern can be recognized, thus we conclude that there is no trace of the crystallization in the nanowire.

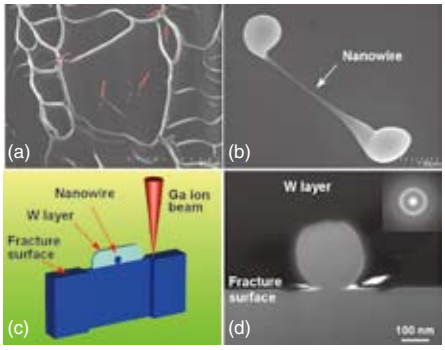

Fig. 1 Nanowires on the fracture surfaces of Zr based BMG. (a) Vein Pattern. (b) 100 nm diameter nanowire. (c) FIB fabrication for TEM observations. (d) TEM image of nanowire cross section.

On the fracture surface, there are not only the nanowires but also the round ridges that configure vein patterns, as seen in Fig. 1(a). To understand structural consequences of the ridges, we used the Ar ion milling to prepare an oblique sectional surface, as illustrated in Fig. 2(a). Figure 2(b) is the SEM image showing both the milled and fractured surfaces. For the left side of the image, the milled surface has featureless and the EDX obtained from this area represents the bulk chemical components of the BMG. For the right side, the prior vein features can be recognized. Remarkably, at the boundary between the milled and fractured surfaces, the ridges as labeled by the white arrows have a tubular structure. Figure 2(c) is the expanded image of the white box in (b). It shows that the inner diameter is 350 nm. Although the cylindrical feature is not a perfect round shape, the image provides the existence of the nanotube on the fracture surface.

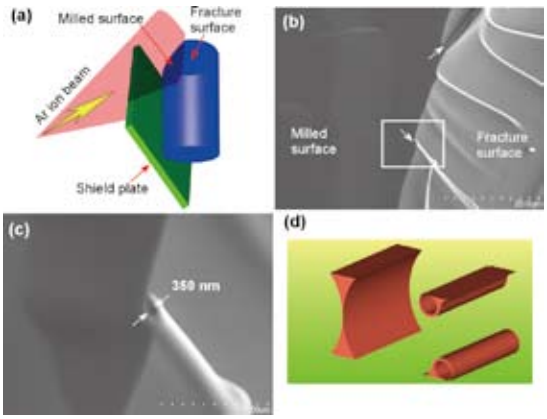

Fig. 2 (a) Schematic diagram of the tilt Ar ion milling method. The Ti shield plate (green) located in front of the fractured sample (blue). The oblique sectional surface was prepared by removing the uncovered area of the shield with Ar ion irradiation (pink). (b) The SEM image represents the boundary between the milled surface (left) and the fracture surface (right). The white arrows indicate the nanotube locations. (c) Higher magnification SEM image of the nanotube was obtained from the white box in (b). (d) 2D meniscus models.

Reference

[1] K. S. Nakayama, Y. Yokoyama, G. Xie, Q. S. Zhang, M. W. Chen, T. Sakurai and A. Inoue, Nano Lett. **8**, 516-519 (2008).

Contact to
Koji S. Nakayama (Research and Development Project on Advanced Metallic Glasses, Inorganic Materials and Joining Technology; Present: WPI-AIMR)
e-mail: kojisn@imr.tohoku.ac.jp

Real-space Structural Studies of Cu-Zr-Ti Glassy Alloy

Structural features of a glassy $Cu_{60}Zr_{30}Ti_{10}$ alloy are studied by using the real-space pair distribution and radial distribution functions. A certain degree of medium-range order in this alloy maintains up to about 2 nm distance. The interatomic distances closely correspond to those of oC68 $Cu_{10}Zr_7$ compound which allows obtaining high relative density of the glassy alloy.

$Cu_{60}Zr_{30}Ti_{10}$ bulk glassy alloy exhibits a high mechanical strength exceeding 2 GPa. In the present work we study the structure of the $Cu_{60}Zr_{30}Ti_{10}$ alloy by using real-space distribution functions. Synchrotron radiation X-ray diffraction in transmission was carried out using a high energy monochromatic beam of the European Synchrotron Radiation Facility equipped with a nitrogen-cooled double-silicon monochromator. High-resolution transmission electron microscopy (HRTEM) investigation was also carried out.

The interference function was calculated from the XRD intensity profile after the necessary corrections while pair distribution PDF (r) and radial distribution RDF(r) functions were obtained by Fourier Transformation (Fig. 1).

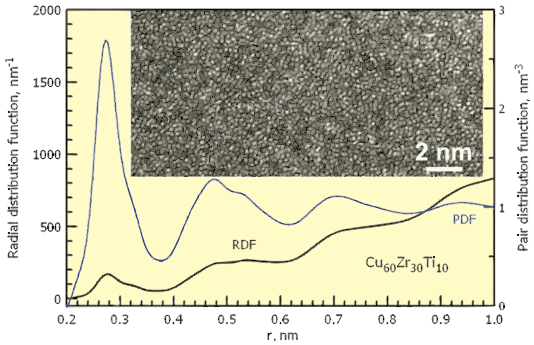

Fig. 1 PDF (r) and RDF(r). The insert – HRTEM image

This is a Cu-rich alloy, the lowest possible Goldschmidt bond length observed in Cu-Cu pair of 0.256 nm is also reflected in the position of the main maximum. However, taking into account large negative mixing enthalpy of the Cu-Zr interatomic pair one can assume that this atomic pair corresponds to the most probable interatomic distance (left shoulder of the PDF function) in the present alloy. The maximum of the left shoulder (0.273 nm) corresponds to somewhat lower value than the Cu-Zr interatomic distance (0.289 nm) predicted by the Goldschmidt atomic radii owing to negative mixing enthalpy in this atomic pair.

Such effect is quite common in the intermetallic compounds. oC68 $Cu_{10}Zr_7$ phase is a stable phase forming in the $Cu_{60}Zr_{30}Ti_{10}$ alloy after crystallization of the glassy phase. It is isomorphous to oC68 $Ni_{10}Zr_7$ one, has close lattice parameters and the Goldschmidt atomic radius of Ni is close to that of Cu. In some clusters this phase shows Ni-Zr distances as small as 0.238 nm and typical Ni-Zr interatomic distances are about 0.26-0.28 nm which is less than 0.289 nm predicted by the Goldschmidt atomic radii but corresponds well to the PDF(r) peak position.

Different Cu-Cu and Cu-Zr interatomic distances observed in the oC68 $Cu_{10}Zr_7$ compound varying in wide ranges from about 0.24 to 0.31 nm for Cu-Zr pair and from about 0.22 to 0.31 for Cu-Cu pair explain the shape of the main PDF(r) maximum (Fig. 1) responsible for the Cu-Cu, Cu-Ti and Cu-Zr atomic pairs. It makes clear why partial distances could not be resolved as the shoulders and disproves the applicability of the Goldschmidt atomic radii approach for complex glassy alloys. The composition of the oC68 $Cu_{10}Zr_7$ phase is different from that of the $Cu_{60}Zr_{30}Ti_{10}$ alloy but the $Cu_{10}(Zr,Ti)_7$ phase is the main structure constituent in this alloy after complete crystallization and can be used as a good approximant to explain structure features of this glassy alloy.

According to Fig. 2 detectable medium-range order maintains until about 2 nm of the interatomic distance independently on the truncation distance of the Fourier Transformation in the reciprocal space. It allows us to anticipate that at the maximum Q value of 160 nm^{-1} used there is no significant influence of the truncation value of the Fourier Transformation of the interference function on the shape of the PDF(r) function and the observed medium-range order until about 2 nm is rather true. Such a high degree of the medium range order is well consistent with recent models which predict that metallic glasses are not random packing of atoms but dense packing of clusters. It is also deduced from the small volume difference between glassy and the corresponding crystalline phases.

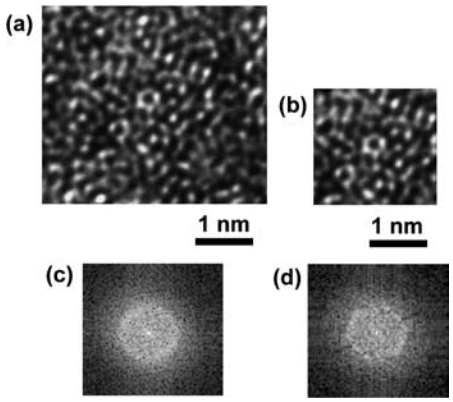

Fig. 2. Two parts of the HRTEM image in Fig. 1: (a) about 16 nm^2 and (b) about 4 nm^2 in size. Area (b) is a part of (a). (c) and (d) are the corresponding FFT images.

A question may arise if the medium-range order maintains until about 2 nm why no clearly ordered zones are seen in the HRTEM image in Fig. 1. If one takes a Fast Fourier Transformation (FFT) of two parts of the HRTEM image like shown in Fig. 2 one can see that although the FFT image shows a diffuse halo only from the area of about 16 nm^2 it has some features if taken from the area of about 4 nm^2. At the same time an icosahedral-type medium range order which is expected to be a dominant local configuration in liquids and metallic glasses may be a good explanation why no crystal-like atomic arrays are observed in the HRTEM images (Figs. 1 and 2) of these glasses [1]. This idea is in a good consistency with the formation of the nanoscale icosahedral phase observed in a Cu-Zr-Ti-Pd alloy on devitrification [2,3].

Thus, the structure of the $Cu_{60}Zr_{30}Ti_{10}$ alloy was studied by real-space distribution functions. The influence of the truncation distance of Fourier Transformation procedure is also studied. It is suggested that the medium-range order in this alloy maintains up to about 2 nm distance. It is also shown that the interatomic distances correspond to those of oC68 $Cu_{10}Zr_7$ compound and illustrated inapplicability of Goldschmidt atomic radii approach to the length of Cu-Zr atomic pair in the glassy phase.

References

[1] S. Ranganathan and A. Inoue: Acta Materialia **54** 3647 (2006).
[2] D. V. Louzguine and A. Inoue: Scripta Mater. **48**, 1325 (2003).
[3] D. V. Louzguine, A. R. Yavari and A. Inoue: Phil. Mag. **83**, 2989 (2003).

Contact to
Dmitri V. Louzguine (R&D Project on Advanced Metallic Glasses, Inorganic Materials and Joining Technology; WPI AIMR.)
e-mail: dml@imr.tohoku.ac.jp

Synthesis of New Cu-Zr-Based Bulk Glassy Alloys with Unusual Glass-Forming Ability

The eutectic $Cu_{36}Zr_{48}Ag_8Al_8$ alloy exhibited unusual glass-forming ability (GFA), the glassy samples with diameters of over 20 mm were fabricated by Cu mold casting and water-quenching [1,2]. The GFA was further enhanced by addition of a small amount of Ni or Pd [3].

The thermal stability of supercooled liquid and GFA of Cu-Zr-Ag alloys remarkably increased by addition of Al. Figure 1 shows the composition dependence of the critical sample diameters (d_c) for the quaternary Cu-Zr-Ag-Al glassy alloys. The d_c above 15.0 mm are obtained by Cu mold casting in a wide composition range of 32 to 42 at% Cu, 42 to 50 at% Zr, 5 to 10 at% Ag, and 5 to 8 at% Al. The quaternary eutectic $Cu_{36}Zr_{48}Ag_8Al_8$ alloy exhibits the largest supercooled liquid region (ΔT_x) of 108 K and the best GFA. Its d_c reaches 25 mm.

Figure 2 (a) shows the outer shape and surface appearance of the $Cu_{36}Zr_{48}Ag_8Al_8$ alloy samples with diameters of 16 and 20 mm produced by water-quenching in no flux melting condition. The surfaces did not exhibit a metallic luster because the surface reacted slightly with water or quartz tube. However, all the surfaces were smooth and neither protuberances nor cavities were observed. The XRD patterns, which were taken from the central region of the cross-section of the rods, consisted of only broad peaks, indicating that a single glassy phase was formed (see Fig. 2(c)). A full eutectic structure consisting of $CuZr_2$, $AlCu_2Zr$, $AgZr_2$ and other unknown phases are formed for water-quenched $Cu_{36}Zr_{48}Ag_8Al_8$ samples with a diameter of 25 mm (see Fig. 2(b, c)). The eutectic structure is very uniform and fine. The average spacing of the eutectic structure in the central region is less than 500 nm. These results suggest that solidification of the eutectic structure occurs via homogeneous nucleation and nuclei growth at a limited rate. This solidified mode of the eutectic alloy seems to promote glass-formation.

The addition of a small amount of Ni or Pd into the $Cu_{36}Zr_{48}Ag_8Al_8$ alloy is effective for further increase in the thermal stability and GFA. Figure 3 shows the outer shape and XRD patterns of the as-cast $Cu_{32}Zr_{48}Ag_8Al_8Ni_4$ and $Cu_{34}Zr_{48}Ag_8Al_8Pd_2$ alloy samples with a diameter of 30 mm. The surface of the samples exhibits a mirror-like luster. The XRD patterns consist of only broad peaks, indicating that the samples are in a glassy state.

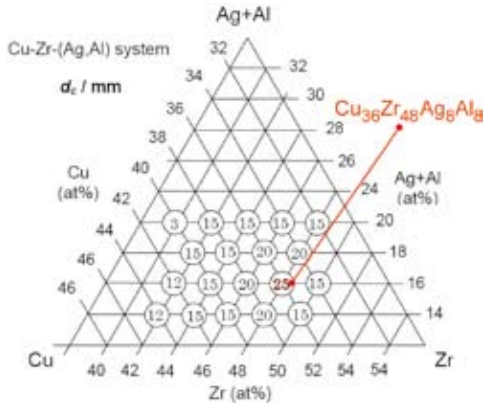

Fig. 1 Composition dependence of the critical sample diameter (d_c) for Cu-Zr-Ag-Al glassy alloys.

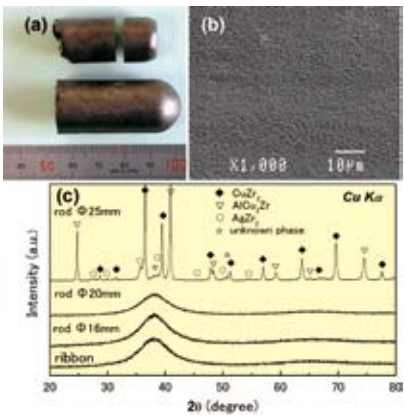

Fig. 2 (a) Outer shape of water-quenched $Cu_{36}Zr_{48}Ag_8Al_8$ alloy samples with diameters of 16 and 20 mm. (b) Cross-sectional structure in the central region of water-quenched alloy sample with a diameter of 25 mm. (c) XRD patterns of the water-quenched alloy samples with diameters of 16, 20 and 25 mm. The data of the melt-spun ribbon are also shown for comparison.

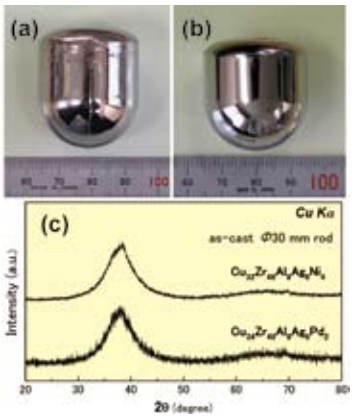

Fig. 3 ((a) and (b)) Outer shape and (c) XRD patterns of as-cast $Cu_{32}Zr_{48}Ag_8Al_8Ni_4$ and $Cu_{34}Zr_{48}Ag_8Al_8Pd_2$ alloy samples with a diameter of 30 mm.

Compared to other bulk glassy alloys with critical diameters above 20 mm, the present alloys can be easily prepared, and exhibit simultaneously large ΔT_x, high corrosion resistance and excellent mechanical properties in conjunction with a lower alloy cost, and thus may enable useful engineering applications in the near future.

References

[1] Q. Zhang, W. Zhang, and A. Inoue, Mater. Trans., **48**, 692 (2007)

[2] W. Zhang, Q. Zhang and A. Inoue, J. Mater. Res., **23**, 1452 (2008).

[3] Q. Zhang, W. Zhang and A. Inoue, Mater. Trans., **48**, 3031 (2007).

Contact to
Wei Zhang (Research and Development Project on Advanced Metallic Glass, Inorganic Materials and Joining Technology)
e-mail: wzhang@imr.tohoku.ac.jp

Structural Evolution of Cr-rich Precipitates in a Cu-Cr-Zr Alloy During Heat Treatment Studied by 3 Dimensional Atom Probe

Structural evolution of nano-precipitates in a Cu-Cr-Zr alloy was studied after aging by laser assisted local electrode 3D atom probe (Laser-LEAP). It clear that after prime aging at 460 ºC, Cr precipitates enriched with Zr. Further overaging (reaging) at 600 ºC caused segregation Zr and impurities of Si and Fe around the Cr precipitates.

Cu–Cr–Zr alloy is expected as potential heat sink material for the International Thermonuclear Experimental Reactor (ITER) divertor [1]. The main problem to be solved is its thermal stability, since the heat treatment during joining procedures of divertor fabrication may cause solution annealing or reaging of the alloy. Furthermore, the effect of Zr on the precipitation behavior is not well understood for the Cu-Cr-Zr system. The question of chemical compositions and the structures around the precipitates in Cu-Cr-Zr also remain unresolved. To clarify the structural evolution of precipitates, we have employed the Laser-LEAP [2].

The test specimens of Cu-0.78 wt% Cr, 0.13 wt% Zr, 0.003 wt% Si, 0.008 wt% Fe were solution annealed (SA) at 960 °C for 3 h and then quenched, followed by prime aging at 460 °C (PA) and reaging at 600 °C for 1(RA1) and 4h (RA2), respectively.

Atom maps of distributions of the solute (Cr and Zr) and impurity (Si and Fe) atoms in the heat-treated (PA, RA1 and RA2) states of the alloy are shown in Figure 1. Cr-rich precipitates are formed in the PA state and coarsen during reaging at 600°C. High number density of fine Cr-rich precipitates were observed by Laser-LEAP.

In the RA1 state the Cr-rich precipitates were coarsened and almost spherical in shape. Zr, Si and Fe atoms segregated around the Cr-rich precipitates [Fig. 1(b)].

During the RA2 reaging the spherical precipitates were coarsened furthermore and Zr, Si and Fe atoms segregated in the interface regions between the precipitates and the matrix [Fig. 1 (c)].

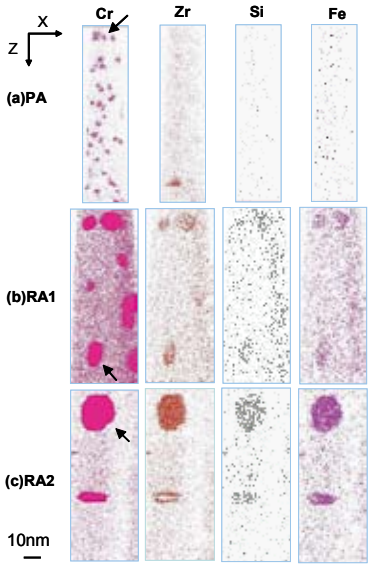

Figure 1. Atom maps of the solute and impurities in the heat-treated states of the Cu-Cr-Zr alloy. The atom maps of the precipitates marked by the arrows are enlarged in Fig. 2.

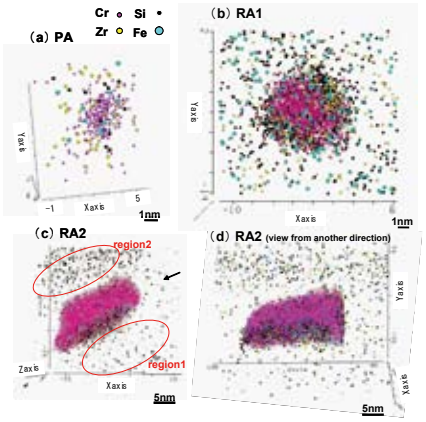

Figure 2. Atom maps along the thinnest direction of the precipitates in the Cu-Cr-Zr alloy. In (d) the projection is done along the other direction shown by the arrow in (c).

Figure 2 shows detailed atom maps around each Cr-rich precipitate in the reaged states marked by the arrows in Fig. 1. In Fig.2 (a), showing a precipitate in the PA state, Zr, Fe and Si atoms were found to be slightly segregate on the interface regions of the Cr-rich core and form an atmosphere of these atoms. In the RA1 state, not only Cr-rich core but also the Zr and Si rich interface layer grew as shown in Fig. 2 (b) The spherical Cr-rich precipitates were sandwiched between two enriched shell regions with Zr, Si and Fe. Concentrations of Zr and Si are about 8 at% at the interfaces, which corresponds to a chemical composition of about Cu_7Cr_3ZrSi.

Figure 2 (c) and (d) shows the atom map of the precipitate in the RA2 state. In some cases, the enriched shell formed only on one side of the Cr core, but almost not on the other side. The concentrations of Zr, Si and Fe in the surrounding “region 1” outside of the enriched shell are lower than that of the “region 2” in Fig. 2(c) due to the segregation to the enriched shell. This segregation of Zr and Si on one side seems to be affected by the strain field around the precipitates. In Cu-Cr-Zr systems, one would expect the incoherency between the Cr-rich precipitates and the matrix to increase with growth of the Cr-rich precipitates. If so, Zr and impurities of Si and Fe might segregate on the interfaces between the Cr-rich precipitates and the matrix and then, form an enriched shell on the other side which relaxes the strain induced by the misfit between the BCC Cr-rich precipitates and the FCC matrix.

References

[1] M. Hatakeyama, H. Watanabe, M. Akiba and N. Yoshida, J. Nucl. Mater. **307-311**, 444 (2002).
[2] M. Hatakeyama, T. Toyama, Y. Nagai and M. Hasegawa, M. Eldrup and B. N. Singh, Mater. Trans. **518-521**, 49 (2008).

Contact
Masahiko Hatakeyama (International Research Center for Nuclear Material Sciense)
e-mail: hatake@imr.tohoku.ac.jp

Ductility Improvement of a Zr-Based Bulk Glassy Alloy by Cold Rolling

New ductile bulk glassy alloy (BGA) with macroscopic tensile elongation has been developed by control of pre-introduced shear band structure with cold rolling. Cold-rolled structure is characterized by the lamellar structure with combination of deformed shear band regions and non-deformed block regions. Since the deformed shear band region can be deformed by lower shear stress than that of non-deformed region, cold rolled bulk glassy alloy can deform homogeneously in macroscopic. By the control of shear band structure, we can obtain ductile BGAs with macroscopic tensile elongation at room temperature.

Cold rolling of BGA is usually required sufficient ductility to introduce high-dense shear bands even at a few percent of reduction ratio. Insufficient ductility brings about accidentally the serious fracture during the cold rolling. Therefore, we have to determine the estimation method of the maximum reduction ratio of cold roll [1]. As a result, the density of cast Zr-based glassy alloy has a good linear relation with maximum reduction ratio of cold rolled samples, as shown in Fig. 1. The density is useful information to estimate the ductility of the cast Zr-based glassy alloy.

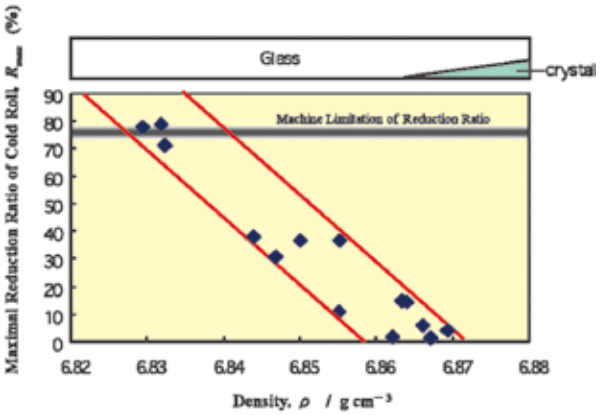

Fig.1 The relationship between the maximum reduction ratio of cold roll and density of cast $Zr_{50}Cu_{30}Ni_{10}Al_{10}$ glassy alloys.

Furthermore, the shear band structure of cold rolled glassy alloy is effective to enhance the ductility and toughness [2], sometimes, which factors are considered as drawbacks in glassy alloys. Especially, little tensile elongation is usually seen in glassy alloys at room temperature, whereas the superior elongation can be seen in compression test of ductile glassy alloys. However, the tensile plastic elongation at room temperature can be obtained by the cold rolling, as shown in Fig. 2. The maximum plastic strain was seen in 10 % cold rolled specimen as about 0.3 % [3]. Figures 3 (a-f) show the over view, magnified fractured surface and side images of the same specimens in Fig. 2. A number of fine steps were seen on the fractured surface (Fig. 3(e)) of the cold rolled glassy alloy, which suggests the reoperation of pre-introduced shear band during the tensile test [4]. This fact means the co-operative shear bands movement originates to the tensile plastic elongation without apparent work softening. In conclude, co-operate movement of a number of pre-introduced shear bands, whose morphology was controlled to be crossed to each other, reveals the distinct tensile plastic elongation.

As the result, the composite-like structural control by cold rolling is a useful process to enhance the toughness and ductility of glassy alloys. The intrinsic ductility of the Zr-based bulk glassy alloy is extremely high [5], that phenomenon can be enhanced much more by the control of shear band structure with the cold rolling process.

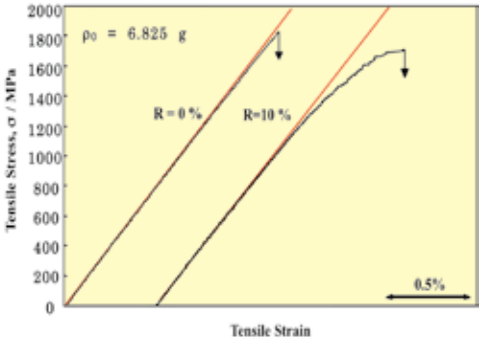

Fig.2 Tensile stress and strain curves of cold rolled $Zr_{50}Cu_{30}Ni_{10}Al_{10}$ glassy alloys with reduction ratios of 0 and 10 %.

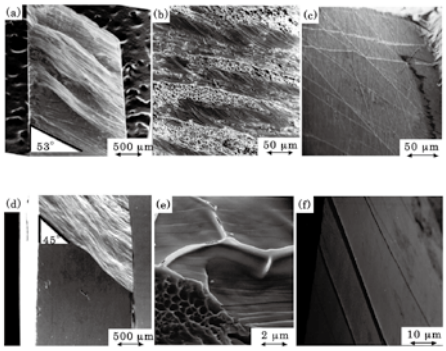

Fig.3 Tensile fractured surface SEM images of non rolled (a~c) and 10% cold rolled (d~f) $Zr_{50}Cu_{30}Ni_{10}Al_{10}$ glassy alloys.

References

[1] Y. Yokoyama, Y. Akeno, T. Yamasaki, P. K. Liaw, R. A. Buchanan, and A. Inoue Mater. Trans., **46**, No12, 2755 (2005).

[2] Y. Yokoyama, K. Yamano, K. Fukaura, H. Sunada and A. Inoue, Mater. Trans., **42**, 623 (2001).

[3] Y. Yokoyama, K Inoue and, K. Fukaura, Mater. Trans., **43**, 3199 (2002).

[4] Y. Yokoyama, The World of Bulk Metallic Glasses and their Composites, ISBN:978-81-308-0196-4 Edited by Can Fang, pp.141 (2007).

[5] N. Yoshida, K. Fujita, Y. Yokoyama, H. Kimura and A. Inoue, J. Jpn. Inst. Metals, **71**, 730 (2007).

Contact to
Yoshihiko Yokoyama (Advanced Research Center of Metallic Glasses)
e-mail: yy@imr.tohoku.ac.jp

Superhydrophilicity and Photocatalytic Activity of TiO_2 Prepared by Anodic Oxidation in Sulfuric Acid Aqueous Solution

TiO_2 photocatalyst has been practically applied and has potentially broad applications in quantitative decomposition or sterilization of chemical substances like endocrine disruptors, injurious volatile compounds, and organic pollutants in water and air. Furthermore, the self-cleaning property of TiO_2 due to superhydrophilicity is useful for photodegrading various noxious or malodorous chemicals.

Anodized TiO_2 oxide on titanium and its alloys has several advantages for controlling the photocatalytic activities by doping through controlling the electrolyte composition, forming stable oxide with adhesion strength at the interface, fabricating porous microstructure with tubular pores and cost performance. The electrochemical parameters such as conversion potential and current density could control the microstructure and constituent phase of the oxide, and influences the photocatalytic activities and superhydrophilicity. High crystallinity of anatase and/or rutile is expected to improve photocatalytic activities because it reduces a number of re-combination sites of electron and hole. An increase of potential and current density generates a sparking due to electric arcs through dielectric breakdown and concurrently porous morphology is produced.

The effects of sulphuric acid concentration on the anatase phase formation and superhydrophilicity revealed that anatase formation is promoted either by an increase in conversion potential or by annealing and that superhydrophilicity is also improved by the above [1]. The mechanism of superhydrophilicity was due to a newly formed oxygen defect; this oxygen defect is formed after the surface oxygen traps two holes that are generated by the photocatalysis reaction as shown in Fig. 1 [2].

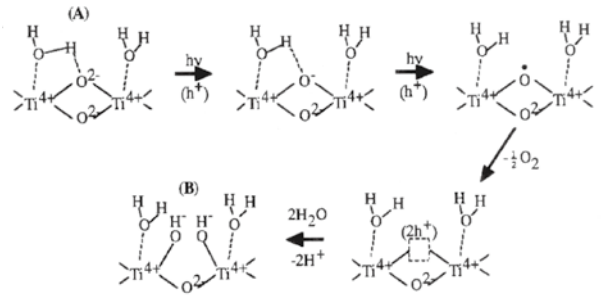

Fig.1 Proposed mechanism of the photoinduced conversion of TiO_2 [2].

All the oxides show an asymmetric O 1s XPS spectrum, and a shoulder band on the higher binding energy side of the main peak originated from the adsorption of hydroxyl groups is observed (Fig. 2). The intensity of the shoulder in the annealed oxide (b) is higher than that in the as-anodized oxide (a). Moreover, the intensity of the shoulder peak increases with UV illumination when it is exposed to oxygen under UV illumination, and it is to air and subsequently subjected to UV illumination, implying that the annealed oxide interacts strongly with the hydroxyl groups. The results suggest that the annealed oxide interacts strongly with the hydroxyl groups.

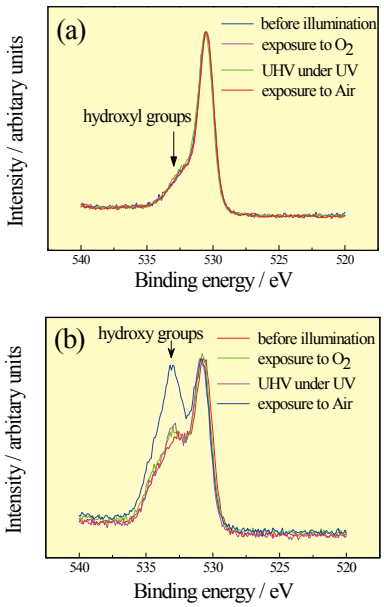

Fig.2 O 1s XPS spectrum of the as-anodized (a) and annealed (b) oxides: before UV illumination, exposure to O_2 for 5 min under illumination, illumination for 30 min and exposure to air for 1 h followed by illumination.

Further increase of the sulfuric acid concentration in the electrolyte generates nano-sized pores (Fig.3), and the predominant oxide phase is replaced from anatase to rutile. The bleaching of methylene blue over the anodized oxide increases with the concentration of sulfuric acid and by annealing. Studies have been under progress [3].

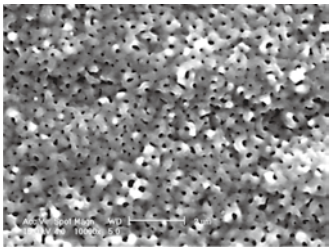

Fig.3 Microstructure of the oxide anodized in 0.1 M the sulfuric acid concentration in the electrolyte.

References

[1] N. Masahashi, S. Semboshi, N. Ohtsu, and M. Oku, to be published in Thin Solids Film (2008).

[2] N. Sakai, A. Fujishima, T. Watanabe, K. Hashimoto, J. Phys. Chem. B **105**, 3023 (2001).

[3] N. Masahashi, Y. Mizukoshi, S. Semboshi and N. Ohtsu, unpublished work (2008).

Contact to
Naoya Masahashi (Osaka Center for Industrial Materials Research)
e-mail: masahasi@imr.tohoku.ac.jp

Nanoimprint of Glassy Alloy for Interference Optical Components

Glassy Alloys (Metallic glasses) are useful for fabricating nanodevices due to their viscosity in the supercooled liquid state and homogeneity on nanometer scales. In this study, we developed interference optical components of the material such as RGB diffraction grating, a hologram and non-reflecting surface by nanoimprint (superplastic nanoforming) with dies fabricated by LIGA process and FIB-nanomachining.

Interference optical components have been fabricated by molding polymer materials because of their precision formability and productivity. However, the materials are not useable at elevated temperatures, and are poorer in mechanical properties and corrosion resistance than metallic materials. Glassy alloys (metallic glasses) are fundamentally amorphous metals and exhibit nanoimprintability due to the Newtonian viscous flow in the supercooled liquid temperature range and homogeneity on nanometer scales. Furthermore, the materials reveal superior mechanical and functional properties, since the materials are promising nanomaterials for mass producing various nanodevices [1]. This study used Pt-based metallic glass with a glass transition temperature of 502 K for fabricating reflective RGB diffraction grating by nanoimprint [2]. A diffraction grating has a fine convex-concave pattern on the surface and is fabricated by nanoimprint with a die. The die was made by Ni-electroforming with master models fabricated by photolithography with one-shot exposure of the interference fringe. An interference optical exposure system has great advantages over the fabrication of nanometer-scale dies by large-area lithography. The light source for the optical system was a solid-state laser (375 nm wavelength), and the fringe pattern interval was determined by the system arrangement. Nanoimprint was carried out with the die. The working temperature of Pt-based metallic glass was 550 K under a compressive stress of 10 MPa. Figure 1 shows the photographs of (a)the die, (b)nanoimprinted RGB diffraction grating and (c),(d),(e)SEM microphotographs of the surface of the grating. The results demonstrated the advantages of the nanoimprint technique on glassy alloys and for mass production of optical components. Similar nanoimprint was performed for fabricating reflection holograms. A hologram sticker was used as the master pattern for fabricating a die. The master pattern was replicated onto the three-dimensional surface microstructure of the die by Ni-electroforming.

Another application of nanoimprint of glassy alloy is a non-refrecting surface [3]. The die was fabricated by nanomachining with focused-ion beam (FIB). FIB-machining characteristics of glassy carbon and Zr-based metallic glass have been studied and are useful for fabricating nano-scale dies because of the isotropic homogeneity of their amorphous structures. Figure 2 (a) illustrates the nanoimprinted surface of Pt-based metallic glass, observed with an optical microscope. We can observe four small areas where there are differences in brightness. Figure 2(b),(c),(d), and (e) present SEM microphotographs of the nano-structured surfaces associated with each small area. The reflectance ratio of these nano-structured surfaces has been measured at λ=533nm and is represented in the figure. The ratio for the surface of Fig.2(c) is only 1 %, since the surface is almost non-reflecting surface. These nano-imprinted, optical components of metallic glasses are useful for numerous applications and under various conditions.

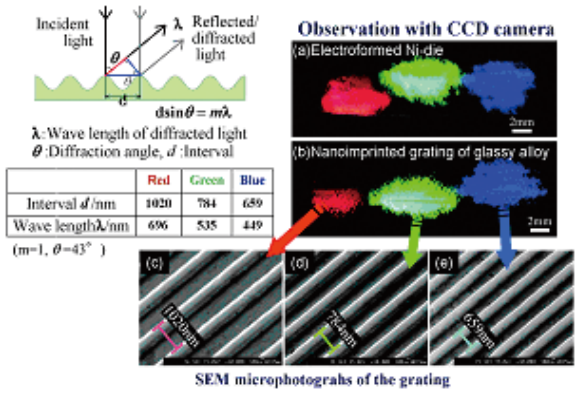

Figure 1 Photographs of (a)electroformed Ni-die, (b)fabricated RGB diffraction grating of Pt-based glassy alloy (metallic glass) by nanoimprint with the die(a), and (c)(d)(e)SEM microphotographs of nanoimprinted surface of the grating(b)

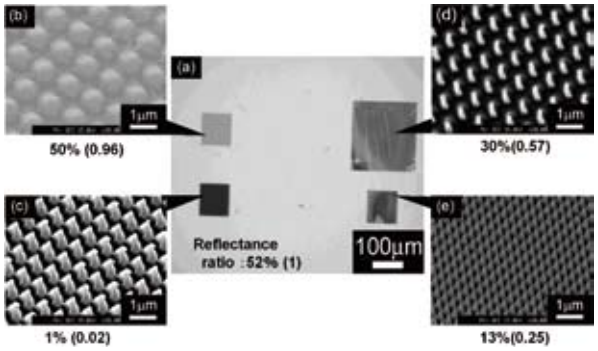

Figure 2 (a)Imprinted surface of Pt-based glassy alloy(metallic glass) observed with an optical microscope and (b)(c)(d)(e)SEM microphotographs of nanostructured surface imprinted on the surface(a). Reflectance ratio was measured at λ=533 nm.

References

[1] P.Sharma, N.Kaushik, H.Kimura, Y.Saotome and A.Inoue, Nanotechnology, **18**, 035302 (2007).

[2] Y. Saotome, Y. Fukuda, I. Yamaguchi and A. Inoue, J. Alloys and Compounds, **434- 435**, 97 (2007).

[3] Y.Saotome, S.Okaniwa, H.Kimura, and A. Inoue, J. Mat. Sci. Forum, **539- 543**, 2088 (2007).

Contact to
Yasunori Saotome(Osaka Center for Industrial Materials Research)
e-mail: saotome@imr.tohoku.ac.jp

Ultra-large Room-temperature Plasticity of a Nanocrystalline Metal

Ultra-large room-temperature plasticity up to 200% true plastic strain is achieved in nanocrystalline (nc) Ni. The low temperature, high strain rate and high flow stress, in conjunction with significant 'cold' nanograin growth, demonstrate that the observed ultra-large plasticity in nc Ni is mainly performed by a grain-boundary-mediated process that is driven by high stresses rather than by thermal diffusion, which is intrinsically dissimilar to that in traditional superplastic materials deformed at high temperatures and low strain rates.

Ultra-large plasticity often occurs at elevated temperatures above 50% of the melting point (T_M) of materials with a slow strain rate (10^{-5} – 10^{-4} s^{-1}). Generally, ultra-large plastic flow of a material is associated with its grain boundary (GB) activities and smaller grains promote the ultra-large plastic flow at lower temperatures and higher strain rates. Thus, as a reasonable extrapolation, room-temperature ultra-large plasticity of nanocrystalline metals, which possess a characteristic grain size less than 100nm, has been expected many years ago. However, nc metals often fail at a tensile strain typically less than 2%, a definitive evidence of whether the ultra-large plastic flow of nc metals can be intrinsically sustained at room temperature still remains missing.

Compression testing of eletrodeposited nc Ni was performed by a newly-developed micro-compression technique. The micro-pillars with nominal diameters ranging from 3 μm to 8 μm and an aspect ratio of 2:1 were prepared by a focused ion beam (FIB) system. A nanoindentation apparatus, equipped with a flat-end diamond indenter, was employed to carry out the room temperature microcompression tests with loading rates ranging from 0.132 mN/s to 13.2 mN/s (the corresponding strain rates range from $4x10^{-3}$ s^{-1} to $5.4x10^{-1}$ s^{-1} during steady plastic flow).

Up to 200% true strain, or 85% loss of its initial height, was surprisingly obtained in nc Ni without neither material nor structural failure (Fig. 1). A typical true stress (σ) vs. true strain (ε) curve of nc Ni strained up to ~100% is shown in Fig. 1b. Steady flow stresses of 2.0 to 2.4 GPa were obtained with loading rates ranging from 0.132 mN/s to 13.2 mN/s. The altering mechanical performances with deformation amounts, i.e. strain softening up to the deformation of about 60% during the steady plastic flow and followed by strain hardening, are found to be associated with the deformation-induced nanostructural evolution.

Visible nanograin growth occurs in the specimens

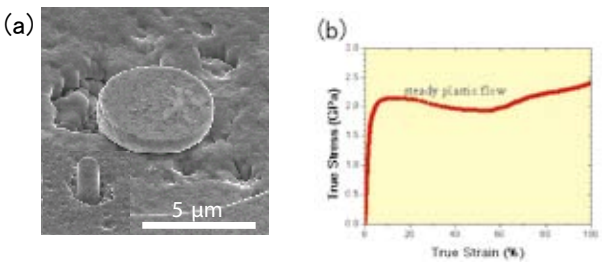

Fig. 1. (a) FIB micrographs of microcompression sample under 200% true strain. The inset is an as-fabricated micropillar. (b) Representative true stress vs. true strain curve of nc nickel subjected to microcompression.

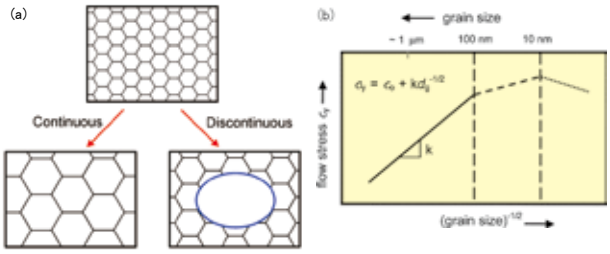

Fig. 2. When the grain size increases due to continuous and/or discontinuous grain growth (a) caused by thermal and/or mechanical activation, yield strength of the material decreases when grain size is larger than 10nm (b).

deformed in the steady plastic flow stage and nanograins remain nearly equiaxial with ~40% plastic deformation. The deformation-induced nanograin growth can lead to enhanced ductility and obvious strain softening in nanocrystalline metals (Fig. 2). In contrast, the microscopic images taken from the sample deformed in the strain-hardening regime (~140% true strain) show coarsened and elongated nanograins that contain a high density of dislocations, stacking faults and deformation twins, indicating intragranular straining of the coarsened nanograins and, thus, strain hardening takes place.

GB sliding takes place mainly via a large number of small local sliding events of atomic clusters that comprises a few or at most a few tens of GB atoms. This stress-enhanced mass transport along GBs, in nature, can lead to ultra-large plastic flow in the absence of enough thermal assistance by high temperatures, accompanied by other atomic-scale GB processes such as nucleation of dislocations. The observed ultra-large plastic flow of nc Ni is thus nearly rate-independent since the dominating deformation mechanism, i.e. stress-enhanced mobility of GB atoms, mainly depends on stress levels rather than time in the case of thermally activated GB diffusion, facilitating the ultra-large plastic flow at high strain rates. In addition, this collective atoms motion at GBs predicted by MD simulations fairly coincides with the measured activation volumes for ultra-large plastic flow and deformation-induced nanograin growth. Accordingly, the nanograin growth and plastic deformation of nc Ni under compression most likely take place simultaneously through stress-enhanced GB motion because both sliding for plastic deformation and migration for nanograin growth are motivated by the mobility or diffusivity of GB atoms.

References

[1] D. Pan, S. Kuwano, T. Fujita and M.W. Chen, Nano Lett. **7**, 2108 (2007).
[2] M. W. Chen and X. Q. Yan, Science **308**, 356c (2005).
[3] D. Pan, T.G. Nieh and M.W. Chen, Appl. Phys. Lett. **88**, 161922 (2006).

Contact to
Mingwei Chen (International Frontier Center for Advanced Materials)
e-mail: mwchen@imr.tohoku.ac.jp

Spontaneous Aggregation of Pentacene Molecules on SAM-treated SiO_2 and Its Influence on FET Characteristics

It has been found that pentacene molecules aggregate spontaneously on the substrates having lower surface energy than that of pentacene (001) surface under ultrahigh vacuum and ambient temperature conditions. In situ AFM-FET measurements have proved that the FET characteristics are significantly affected by this aggregation.

Pentacene ($C_{14}H_{22}$, Fig. 1) is one of the most promising organic semiconductors for organic field effect transistors (OFETs). In order to improve the FET performance, the surfaces of gate insulator, such as SiO_2, are commonly modified by the self-assembled monolayers (SAMs), such as hexamethyldisilazane (HMDS) or octadecyltrichlorosilane (OTS) (Fig. 1(c)). Owing to utilization of these SAMs, the performance of the pentacene FET has already exceeded that of amorphous Si FET. There remain, however, crucial problems for practical application, namely, stability and reproducibility of their characteristics. In the present study, we have found spontaneous aggregation of pentacene molecules deposited on SAM-treated SiO_2 substrates under ultrahigh vacuum and ambient temperature conditions (Fig. 2) [1]. *In situ* and real-time observation of growth and the aggregation of pentacene molecules with low-energy electron microscopy (LEEM) revealed that the balance of surface energy between pentacene film and substrate is an origin of this aggregation. Pentacene films grown on the HMDS- or OTS-treated surfaces, which have lower surface energy than that of pentacene (001) surface, tend to aggregate, while those grown on the clean-SiO_2 surfaces, which have higher surface energy, do not aggregate (Fig. 2(a-c)). We constructed an *in situ* atomic force microscopy (AFM)-FET measurement system to find that the FET mobility is significantly affected by the aggregation of pentacene molecules (Fig. 2(d)). Since we have also observed significant degradation of FET performance even in the case of thicker pentacene films, this spontaneous aggregation should be one of the major causes of the instability and irreproducibility of pentacene-based devices.

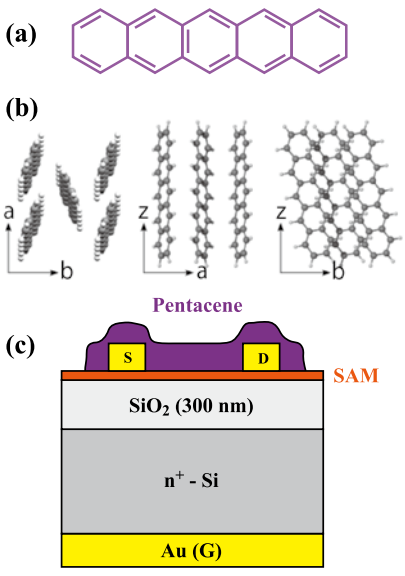

Fig. 1. (a) Molecular structure of pentacene. (b) Crystal structure of the pentacene thin film. (c) Schematics of the sample used for *in situ* AFM-FET measurements.

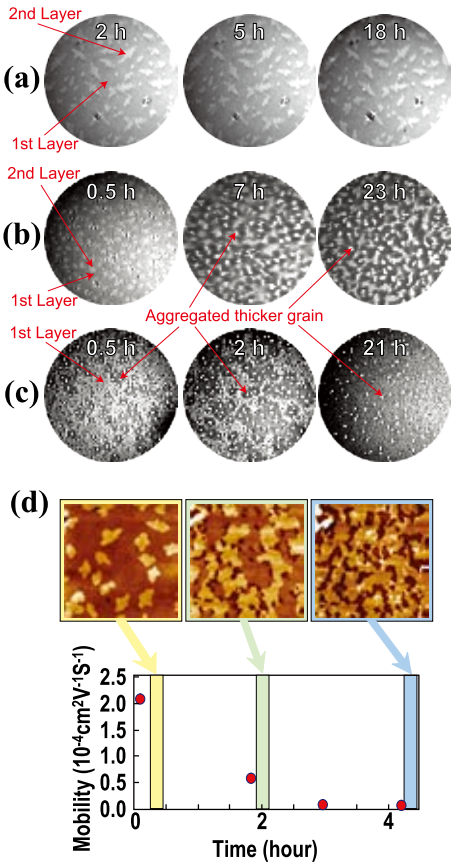

Fig. 2. Morphological change of 1.3 ML-thick pentacene films grown on (a) clean SiO_2, (b) HMDS, and (c) OTS observed with LEEM under UHV and ambient temperature conditions. Elapsed time after deposition is indicated at the top of each figure. Thickness of pentacene film in each region is indicated in the figures. (d) Change of morphology and FET characteristics of 1.3 ML-thick pentacene film measured with *in situ* AFM-FET system under high vacuum and ambient temperature conditions. The size of AFM images is 4.8x4.8 μm^2.

Reference

[1] G. Yoshikawa, J. T. Sadowski, A. Al-Mahboob, Y. Fujikawa, T. Sakurai, Y. Tsuruma, S. Ikeda and K. Saiki, Appl. Phys. Lett. 90, 251906 (2007).

Contact to
Genki Yoshikawa (SAKURAI Project, International Frontier Center for Advanced Materials)
e-mail: yoshik-0@imr.tohoku.ac.jp